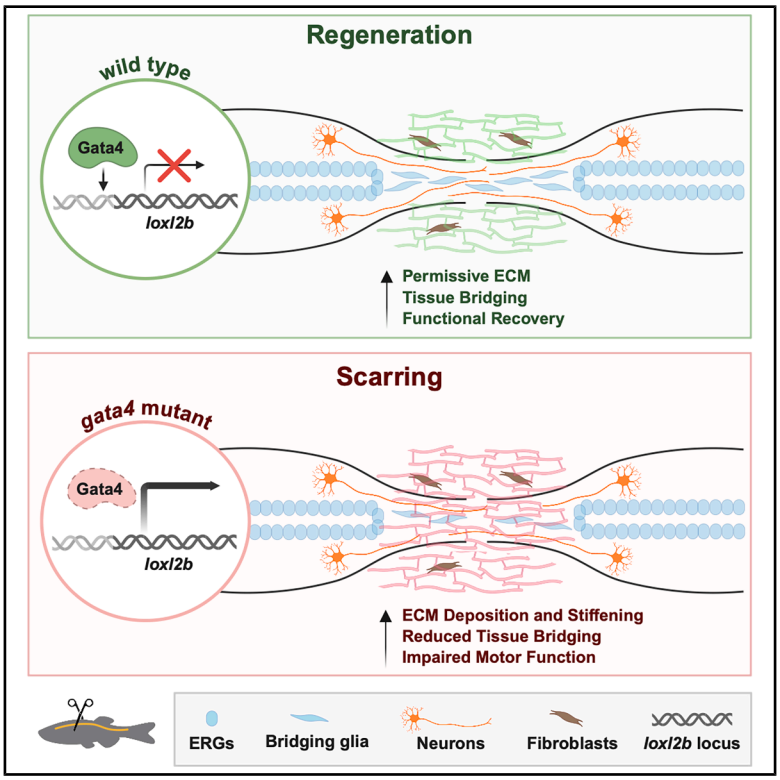
Cell Reports

Article

A Gata4–Loxl2 axis controls ECM remodeling to enable scar-free spinal cord regeneration in zebrafish

Graphical abstract



Highlights

- Gata4 enables scar-free spinal cord regeneration in zebrafish
- Loss of Gata4 promotes Loxl2b-dependent collagen cross-linking and fibrosis
- Loxl2b inhibition restores tissue bridging and motor recovery in *gata4* mutants
- Hif-1α signaling contributes to injury-induced activation of *gata4*

Authors

Nicolas P. Noel, Vânia F. Lima Fernandes, Andrew Kjar, ..., Eman A. Akam-Baxter, Ethan S. Lippmann, Valentina Cigliola

Correspondence

valentina.cigliola@vanderbilt.edu

In brief

Fibrotic scar formation prevents successful spinal cord regeneration in mammals. Noel et al. identify a Gata4–Loxl2 signaling axis that suppresses pathological extracellular matrix remodeling and enables scar-free regeneration in zebrafish.

Noel et al., 2026, Cell Reports *45*, 118050
October 27, 2026 © 2026 The Authors. Published by Elsevier Inc.
https://doi.org/10.1016/j.celrep.2026.118050

CellPress

Cell Reports

CellPress
OPEN ACCESS

Article

A Gata4–Loxl2 axis controls ECM remodeling to enable scar-free spinal cord regeneration in zebrafish

Nicolas P. Noel,[1,2] Vânia F. Lima Fernandes,[3,4] Andrew Kjar,[5] Paige E. Pfotenhauer,[1,2] Hyosung Kim,[5] Mawusi P. Sefogbe,[6] Eman A. Akam-Baxter,[6] Ethan S. Lippmann,[5] and Valentina Cigliola[1,2,3,7,*]

[1]Department of Pharmacology, Vanderbilt University, Nashville, TN 37232, USA
[2]Vanderbilt Brain Institute, Vanderbilt University, Nashville, TN 37232, USA
[3]Université Côte d'Azur, CNRS, Inserm, Institut de Biologie Valrose (iBV), 06108 Nice, France
[4]Université Côte d'Azur, CNRS, Inserm, Institute of Research on Cancer and Ageing of Nice (IRCAN), 06108 Nice, France
[5]Department of Biomedical Engineering, Vanderbilt University, Nashville, TN 37232, USA
[6]Cardiovascular Research Center, Massachusetts General Hospital, Harvard Medical School, Boston, MA 02129, USA
[7]Lead contact
*Correspondence: valentina.cigliola@vanderbilt.edu
https://doi.org/10.1016/j.celrep.2026.118050

SUMMARY

Spinal cord injury in mammals triggers fibrotic scar formation that impedes axon regrowth, whereas zebrafish regenerate and recover motor function without persistent fibrosis. Here, we identify the transcription factor Gata4 as a regulator of regeneration-associated extracellular matrix (ECM) remodeling. Following injury, *gata4* is induced predominantly in ependymo-radial glial cells (ERGs). Gata4 preserves ERG identity and suppresses a fibroblast-like transcriptional program enriched for ECM genes. Loss of Gata4 increases expression of the collagen cross-linking enzyme Loxl2b, resulting in excessive collagen cross-linking, matrix stiffening, and a regeneration-inhibitory ECM environment. These changes delay glial and axonal bridging and impair motor recovery. Pharmacological inhibition of Loxl2b rescues ECM organization, tissue bridging, and functional recovery. Injury-induced *gata4* expression depends in part on Hif-1α signaling and activation of an injury-responsive *cis*-regulatory element. Together, these findings identify a Gata4–Loxl2b axis linking glial cell state to ECM mechanics during spinal cord regeneration.

INTRODUCTION

Spinal cord injury (SCI) causes profound neuronal loss, axonal disruption, and synapse elimination, leading to permanent sensory, motor, and autonomic deficits in mammals. Beyond the initial mechanical insult, secondary injury responses, including immune-cell infiltration, activation of resident glia, and recruitment of mesenchymal cell types, drive the formation of a multicellular injury scar.[1,2] This scar consists of a fibrotic lesion core surrounded by a glial border, and it fundamentally shapes the post-injury environment encountered by regenerating axons.[1,2] The fibrotic lesion core forms due to excessive extracellular matrix (ECM) deposition by invading non-neural cells, particularly fibroblasts. This dense matrix alters biochemical and mechanical properties of the tissue, thereby restricting axonal regrowth.[3–5] Reactive astrocytes and microglia at the lesion border stabilize the injury, support restoration of the blood-spinal cord barrier, and form a glial boundary that segregates spared tissue from the lesion.[1,2] Astrocytes also deposit inhibitory ECM components, including chondroitin-sulfate proteoglycans and tenascin-C, at this border, further influencing the inhibitory post-injury environment.[6–8] Reducing ECM deposition from fibroblasts or astrocytes, or selectively removing inhibitory ECM components, increases lesion permissiveness and facilitates axonal regeneration.[1,5,9,10]

In contrast to mammals, zebrafish possess a remarkable capacity to regenerate the spinal cord and recover motor function throughout life.[11–15] Following SCI in adult zebrafish, fibroblasts contribute to a regeneration-permissive ECM characterized by restricted accumulation of inhibitory components, including several small leucine-rich proteoglycans.[16,17] Myoseptal and perivascular *pdgfrb*$^{+}$ fibroblasts are a major source of injury-associated ECM.[18] In larval zebrafish, some of these cells have been shown to biphasically regulate inflammation after SCI by interacting with innate immune cells, first promoting and then resolving the acute inflammatory phase, thereby creating conditions that support regeneration.[19] In addition, in adult zebrafish, ependymo-radial glial cells (ERGs), progenitor cells lining the central canal, proliferate after injury, with a subset contributing to the formation of a glial bridge across the lesion site, which has been proposed to provide structural support for axon regrowth.[13,20] Together, a permissive ECM, glial bridging, and tightly regulated inflammation create an environment that actively supports axon regeneration. However, the transcriptional programs linking fibroblast and glial responses to ECM remodeling and a regeneration-permissive niche remain largely unknown.

This is an open access article under the CC BY-NC-ND license (http://creativecommons.org/licenses/by-nc-nd/4.0/).

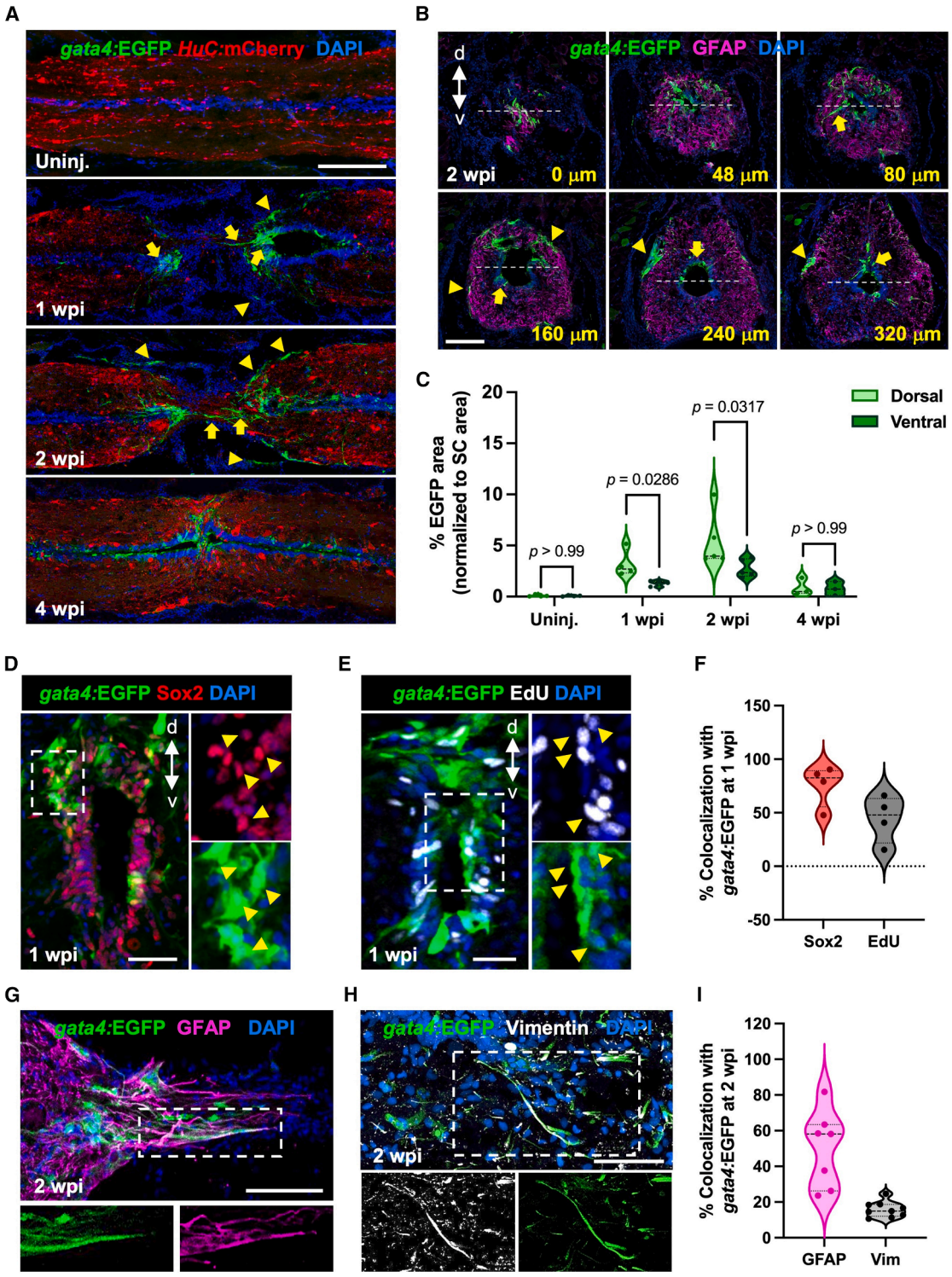


Figure 1. Gata4 regulatory sequences are induced during spinal cord regeneration

(A) *Tg(-14.8gata4:EGFP)* reporter expression (green) in longitudinal sections from uninjured and 1, 2, and 4 weeks post-injury (wpi) animals. *Tg(HuC:*mCherry*)* marks neurons. Arrows and arrowheads indicate EGFP$^+$ cells in and around the regenerating site, respectively.

(B and C) *gata4*:EGFP (green) and GFAP (magenta) expression in transverse sections along the proximodistal axis (B) and quantification of reporter signal in dorsal and ventral regions at 2 wpi (C). Dashed lines delineate the central canal midline; yellow values indicate distance from the injury site. SC, spinal cord.

(D–F) Sox2 (red) (D) and EdU (white) (E) labeling in transverse spinal cord sections from *Tg(-14.8gata4:EGFP)* animals at 1 wpi and percentage of *gata4*:EGFP$^+$ cells positive for Sox2 or EdU (F).

(legend continued on next page)

GATA4, a member of the GATA family of transcription factors (TFs), has emerged as a potent regulator of tissue repair, generally acting in a pro-regenerative manner. The vertebrate GATA family comprises six TFs sharing a conserved two-zinc-finger DNA-binding domain recognizing the consensus motif (A/T)GATA(A/G) or W-GATA-R. GATA4 has received extensive attention for its role in tissue regeneration, particularly in the heart. It is induced in zebrafish cardiomyocytes after ventricular resection injury and marks a population that contributes to myocardial regeneration.[21] In neonatal mice, GATA4 is required for heart repair, and its deletion impairs regeneration, reduces cardiomyocyte proliferation, and increases scar size.[22] Mechanistically, GATA4 controls expression of cell-cycle regulators (e.g., Cyclin A2, Cyclin D2, and CDK4) and of pro-regenerative paracrine factors such as FGF16.[22,23] Beyond the heart, GATA4 also regulates tissue remodeling and anti-fibrotic responses in the liver. In hepatic stellate cells, GATA4 promotes fibrosis regression by repressing fibrogenic genes and activating anti-fibrotic transcriptional programs, and endothelial GATA4 prevents pathogenic remodeling and supports tissue regeneration.[24–27] Emerging evidence indicates that GATA4 is expressed in neurons and glia in the human and murine adult central nervous system (CNS) and regulates astrocyte proliferation and apoptosis *in vitro*.[28] Its loss in human astrocytes is associated with malignant transformation, suggesting that GATA4 regulates glial cell state and may more broadly influence glial responses in the CNS.[29] Thus, GATA4 emerges as a candidate transcriptional orchestrator of proliferation, cell state plasticity, and repair across multiple organs, including the CNS.

Here, we identify Gata4 as a regulator of spinal cord regeneration in adult zebrafish, acting primarily in ERGs around the central canal, which extend processes toward sites of tissue bridging, and to a lesser extent in fibroblasts surrounding the lesion site. Following injury, Gata4 is strongly upregulated and controls expression of lysyl oxidase-like 2b (Loxl2b), an enzyme that normally contributes to ECM structure. Loss of Gata4 function increases Loxl2b levels, leading to excessive collagen cross-linking that stiffens the matrix and creates an anti-regenerative environment, impairing axon growth and functional recovery. Injury-induced *gata4* expression depends, at least in part, on Hif-1α signaling and a short upstream enhancer that harbors Hif-1α binding sites. These findings establish Gata4 as a transcriptional link between injury sensing, glial cell state, and ECM mechanics, revealing how regenerative central nervous systems suppress pathological matrix remodeling and fibrotic scar formation to enable regeneration.

RESULTS

gata4 regulatory sequences are activated during spinal cord regeneration

In a screen for regulators of zebrafish spinal cord regeneration, we identified *gata4* regulatory sequences as being strongly activated after injury. *In situ* hybridization (ISH) revealed negligible endogenous *gata4* transcripts in the uninjured spinal cord, in contrast to a sharp increase in *gata4*-expressing cells around the central canal and a moderate increase throughout the spinal cord following transection injury (Figure S1A). To visualize this response more precisely, we examined spinal cords of *Tg(-14.8gata4:EGFP)* zebrafish, carrying a *gata4* upstream regulatory region extensively shown to recapitulate the endogenous *gata4* expression pattern (Figure S1B).[30] In uninjured tissue, enhanced green fluorescent protein (EGFP) expression was largely undetectable, and sporadically limited to neurons identified by expression of the HuC/D marker (Figures 1A and S1C). At 1 week post-injury (wpi), *gata4*-driven EGFP was detected near the rostral and caudal injury stumps, in cells scattered along the central canal, and in a small population of flattened cells surrounding the spinal cord (Figures 1A and 1B, yellow arrows and arrowheads, respectively). EGFP signal intensified and peaked at 2 wpi, with EGFP-positive cells present at sites of tissue bridging, and decreased by 4 wpi as regeneration progressed (Figure 1A). Cross-sectional analyses at 1 and 2 wpi showed *gata4*-driven EGFP expression primarily confined to ERGs surrounding the central canal and extending into the dorsal spinal parenchyma (Figures 1B and 1C).

To define the identity of *gata4*-expressing cells during regeneration, we conducted histological and molecular analyses using antibodies and transgenic markers. At 1 wpi, most Gata4$^+$ cells co-expressed Sox2, a marker of ERGs (Figures 1D and 1F), and nearly half (44.3%) showed evidence of cell cycling based on 5-ethynyl-2′-deoxyuridine (EdU) incorporation (Figures 1E and 1F). By 2 wpi, approximately half of Gata4$^+$ cells expressed the glial marker GFAP (Figures 1G, 1I, S1D, and S1E), while a minority (15.8%) expressed vimentin, an intermediate filament protein previously shown to be upregulated in ERGs acquiring a migratory phenotype[31] (Figures 1H and 1I). As GFAP immunostaining primarily labels glial processes rather than cell bodies, the degree of GFAP colocalization is likely underestimated. Gata4$^+$ cells co-expressing *olig2*:EGFP, marking progenitors associated with oligodendrocyte and motor neuron lineages,[12] were observed very rarely at 2 wpi (Figure S1F). At this same time point, ∼2% of *gata4*:EGFP$^+$ cells co-localized with *pdgfrb*:mCherry, indicating that *gata4* is expressed in a subset of injury-associated fibroblasts. These cells represent only a minor fraction of the overall Gata4-expressing population (Figures S1G and S1H).

All six GATA TFs remain poorly characterized functionally in the CNS. We probed *gata* gene expression in a published transcriptomic dataset containing ten GFAP$^+$ glial subpopulations at 1 wpi[32] and found that *gata3*, *gata4*, *gata5*, and *gata6* showed distinct patterns of expression across these populations. Notably, *gata4* expression was enriched in two of the ten glial clusters, clusters 1 and 2 (Figure S1I), consistent with our histological analyses showing *gata4* expression in a majority of, but not all, glial cells (Figures 1G, 1I, S1D, and S1E). Overall, our data identify *gata4* as a regeneration-responsive gene

(G–I) GFAP (magenta) (G) and vimentin (white) (H) labeling in longitudinal spinal cord sections from *Tg(-14.8gata4:EGFP)* animals at 2 wpi and quantification of *gata4:*EGFP$^+$ cells positive for GFAP or Vimentin (I). Each dot in (C, F, and I) represents one animal. Dashed boxes in (D, E, G, and H) indicate magnified regions. Mann-Whitney test (C). Scale bars, 200 μm (A), 100 μm (B), 50 μm (D, E, G, and H). d dorsal, v ventral.
Violin plots show the data distribution; dashed lines denote medians and dotted lines denote the 25th and 75th percentiles.

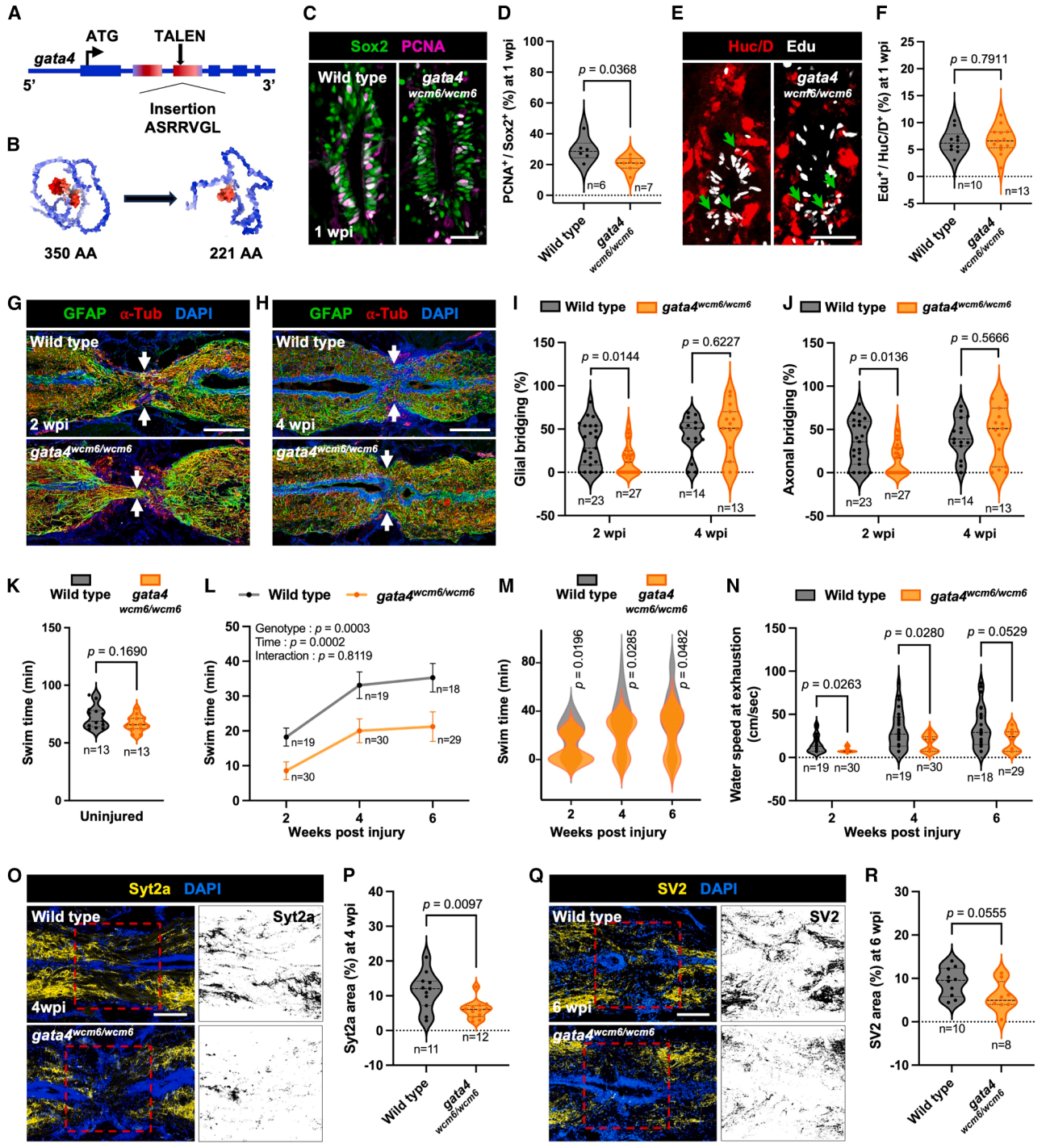


Figure 2. Gata4 loss-of-function delays tissue bridging and impairs motor recovery after spinal cord injury

(A) TALEN insertion in the second *gata4* zinc finger domain of *gata4*$^{wcm6/wcm6}$ zebrafish.

(B) AlphaFold representation of wild-type and *gata4*$^{wcm6/wcm6}$ Gata4 proteins. AA, amino acid.

(C and D) Sox2 and PCNA immunostaining (C) and quantification of ependymal cell proliferation (D) in transverse spinal cord sections of wild-type and *gata4*$^{wcm6/wcm6}$ zebrafish at 1 week post-injury (wpi).

(E and F) HuC/D and EdU staining (E) and quantification of EdU-labeled neurons (F) in transverse spinal cord sections at 1 wpi.

(G–J) GFAP (green) and acetylated α-tubulin (red) staining in longitudinal spinal cord sections at 2 (G) and 4 (H) wpi, and quantification of glial (I) and axonal bridging (J).

(legend continued on next page)

predominantly expressed in ERGs, including those extending processes at sites of tissue bridging.

Gata4 loss-of-function delays spinal cord regeneration and impairs functional recovery

To evaluate the requirement for Gata4 during regeneration, we used *gata4*$^{wcm6/wcm6}$ zebrafish, carrying a 6-bp TALEN-mediated insertion that introduces a premature stop codon at the start of the C-terminal GATA4 zinc-finger domain, eliminating DNA-binding capability[33] (Figures 2A, 2B, and S2A). Uninjured *gata4*$^{wcm6/wcm6}$ embryos appeared phenotypically normal and survived to adulthood without overt morphological abnormalities, although *gata4* null mutants were recovered at sub-Mendelian frequencies, as previously shown.[33]

We subjected *gata4*$^{wcm6/wcm6}$ animals to SCI and histologically and functionally assessed regeneration at multiple timepoints. The *gata4*$^{wcm6/wcm6}$ animals showed a nearly 30% reduction in Sox2^{+} ERG proliferation at 1 wpi compared to wild-type clutch-mates, assessed by PCNA staining on cross-sections ($p = 0.0368$, Welch's *t* test) (Figures 2C and 2D). Injury-induced neurogenesis was not significantly altered in *gata4*$^{wcm6/wcm6}$ animals, as determined by quantification of EdU incorporation into HuC/D^{+} neurons at 1 wpi (Figures 2E and 2F). We then examined glial and axonal bridging across the lesion site on longitudinal spinal cord sections at 2 wpi, using GFAP as a glial marker, and acetylated α-tubulin as an axonal marker. The average diameter of the glial and axonal bridge was reduced by 52.1% and 51.4%, respectively, in *gata4*$^{wcm6/wcm6}$ animals compared to wild type (Figures 2G, 2I, 2J, and S2B). These deficits were no longer detectable by 4 wpi, when tissue bridge measurements in *gata4*$^{wcm6/wcm6}$ animals equaled those of wild types (Figures 2H–2J).

To assess spinal cord function, we quantified swim capacity using a ramped-current swim challenge in which fish swam against progressively increasing water current velocity until failure. The time to failure and the corresponding current velocity were recorded as quantitative measures of swim capacity. While no significant difference in swim capacity was detected between uninjured *gata4*$^{wcm6/wcm6}$ and wild-type animals (Figure 2K), *gata4*$^{wcm6/wcm6}$ fish exhibited significantly reduced swimming endurance at 2, 4, and 6 weeks following SCI (Figure 2L; data distribution in Figure 2M). Although swimming speed of *gata4*$^{wcm6/wcm6}$ animals improved over time, it remained considerably lower than in wild-type animals (Figure 2N). Strikingly, despite recovery of tissue bridging by 4 wpi (Figures 2H–2J), swim defects persisted and remained evident at 10 wpi (Figure S2C), suggesting that factors beyond tissue bridging limit motor function recovery. Overall, these results demonstrate that Gata4 function is required for effective spinal cord regeneration and full recovery of motor function.

Long-term Gata4 loss-of-function alters spinal curvature and synaptic organization

To investigate potential factors contributing to the persistent functional deficits, we next examined whether chronic structural and synaptic abnormalities accompany regeneration in *gata4*$^{wcm6/wcm6}$ zebrafish. Since spinal curvature defects are frequently observed during and after regeneration and can affect swimming performance,[34] we assessed post-injury scoliosis in mutants and wild types at 2, 4, and 6 wpi. For both *gata4*$^{wcm6/wcm6}$ and wild type, no significant differences were detected before injury or up to 4 wpi; however, by 6 wpi, *gata4*$^{wcm6/wcm6}$ animals developed a pronounced spinal curvature ($p = 0.0157$, Mann-Whitney) (Figures S2D and S2E). To determine whether these structural alterations also affected synaptic organization, we examined the distribution of the presynaptic markers Syt2a and SV2. Analyses of the lesion site revealed significantly reduced Syt2a immunoreactivity at 4 wpi and SV2 at 6 wpi in *gata4*$^{wcm6/wcm6}$ spinal cords compared with wild-type fish (Figures 2O–2R). However, when the analysis was restricted to regenerated descending axons labeled by biocytin anterograde tracing and examined immediately caudal to the lesion, no significant difference in Syt2a^{+} puncta was detected between genotypes (Figures S2F and S2G; $p = 0.4286$). These findings suggest that although overall synaptic marker abundance is reduced in mutant spinal cords, presynaptic specialization of regenerated descending axons is largely preserved, pointing instead to broader alterations in synaptic organization within the injured tissue. Collectively, these findings indicate that chronic Gata4 loss-of-function is associated with persistent structural spinal abnormalities and altered synaptic organization following SCI.

Gata4 loss-of-function alters ERG transcriptional programs toward a fibroblast-like, ECM-associated profile

To further characterize the *gata4*$^{wcm6/wcm6}$ phenotype, we performed single-nucleus RNA sequencing (snRNA-seq) of wild-type and *gata4*$^{wcm6/wcm6}$ spinal cords at 2 wpi, when *gata4* expression is maximal (Figures 3A and S3A). Unsupervised clustering of 4,626 nuclei identified 20 cell clusters, including major spinal cord cell types, fibroblasts, and immune cells, distinguished by specific hallmark genes (Figures 3B and S3C). Cell-cluster composition was similar between genotypes, with no substantial differences in the relative proportions of cell types (Figure S3B). Because Gata4 is expressed predominantly in ERGs after SCI (Figure 1; Figure S1), we next used a volcano plot to visualize transcriptional differences between *gata4*$^{wcm6/wcm6}$ and wild-type ERGs (Figure 3C). This comparison revealed widespread transcriptomic changes after *gata4* loss-of-function, with gene-expression profiles differing markedly between genotypes (Table S1). Notably, one of the most strongly

(K–N) Endurance swim capacity of uninjured (K) and injured (L–N) wild-type and *gata4*$^{wcm6/wcm6}$ zebrafish. (M) Distribution of swim capacity at 2, 4, and 6 wpi. (N) Water current velocity at swim failure.
(O and P) Syt2a (yellow) immunoreactivity at 4 wpi (O) and quantification within the lesion and adjacent spinal cord (P).
(Q and R) SV2 immunoreactivity (yellow) at 6 wpi (Q) and quantification (R).
Violin plots show the data distribution; dashed lines denote medians and dotted lines denote the 25th and 75th percentiles. Data in (L) are represented as mean ± SEM. Each dot in (D, F, I–K, N, P, and R) represents one animal. Scale bars, 50 μm (C and E) and 100 μm (G, H, O, and Q). Welch's *t* test (D, F, P, and R); Mann-Whitney test (I–K, M, and N); two-way ANOVA (L).

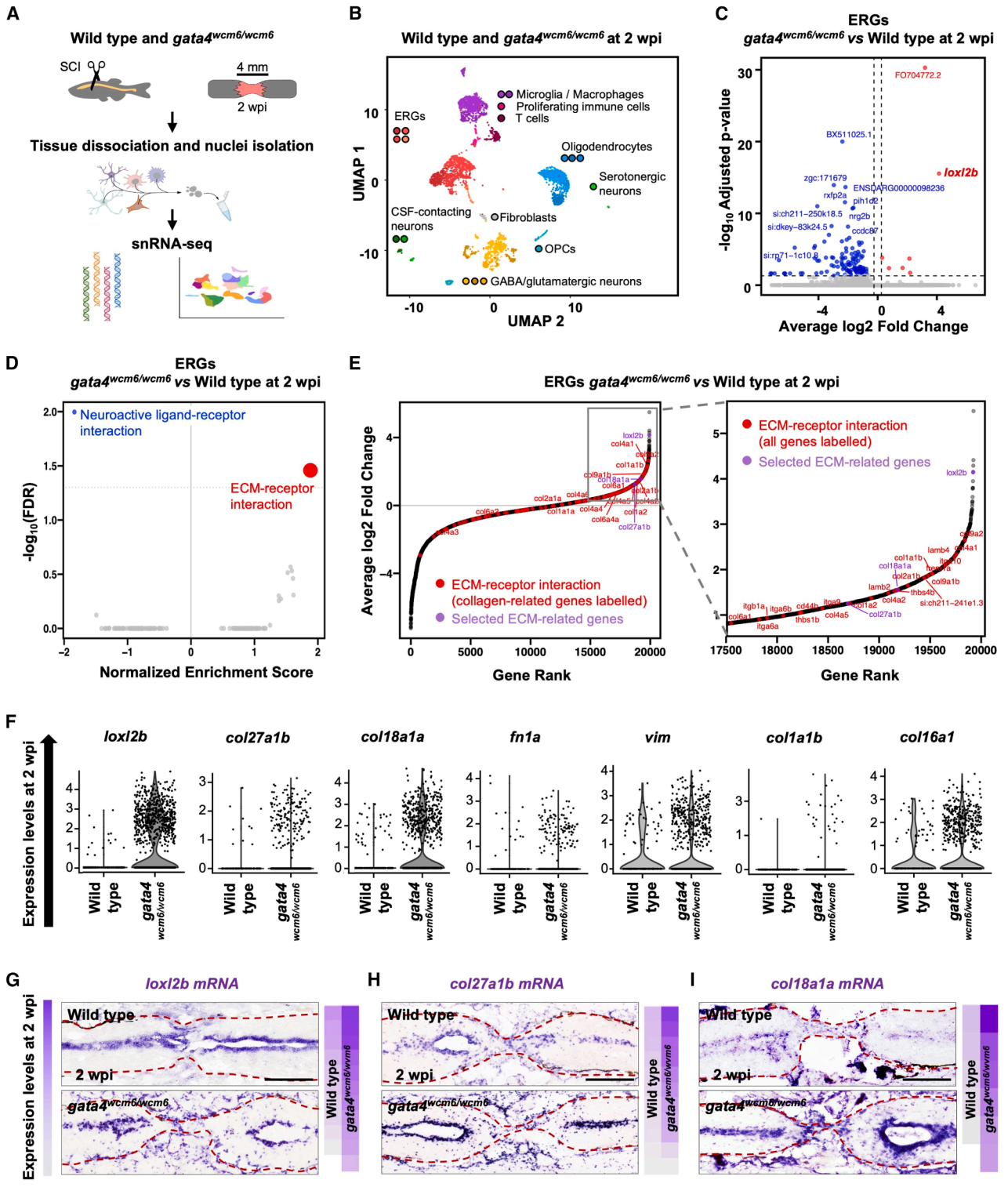


Figure 3. Gata4 loss-of-function induces expression of ECM-related genes in ERGs

(A) Single-nucleus RNA-sequencing (snRNA-seq) strategy.

(B) UMAP of snRNA-seq data at 2 weeks post-injury (wpi), showing identified cell populations from wild-type and *gata4*$^{wcm6/wcm6}$ spinal cords.

(C) Differentially expressed genes in *gata4*$^{wcm6/wcm6}$ versus wild-type ERGs.

(D) Gene set enrichment analysis (GSEA) of KEGG pathways in *gata4*$^{wcm6/wcm6}$ ERGs versus wild-type ERGs.

(legend continued on next page)

upregulated genes in *gata4*$^{wcm6/wcm6}$ ERGs was *lysyl oxidase-like 2b (loxl2b),* which encodes an extracellular enzyme involved in collagen and elastin crosslinking and ECM remodeling (Figure 3C). Gene set enrichment analysis (GSEA) revealed enrichment of ECM-related genes, including those involved in ECM-receptor interactions, in *gata4*$^{wcm6/wcm6}$ ERGs (Figure 3D; Table S2). No enrichment was observed in oligodendrocyte, immune, or neural clusters, and the fibroblast cluster contained insufficient cells for comparison (Figures S3D–S3F). Upregulated genes included multiple collagens, laminins, integrins, and matrix-associated proteins (Figures 3E, 3F, S4A and S4B). We validated expression of three ECM-related transcripts by ISH on spinal cord tissue sections of *gata4*$^{wcm6/wcm6}$ and wild types. In uninjured spinal cords, *loxl2b*, *col27a1b,* and *col18a1a* showed basal expression in cells surrounding the central canal (Figure S5A). Following injury, expression of these transcripts was upregulated and higher in *gata4*$^{wcm6/wcm6}$ spinal cords than in wild-type controls, in and around the lesion site (Figures 3G–3I). Expression of *loxl2b*—the most highly upregulated transcript in our RNA-seq dataset—in *gata4*-expressing cells was further confirmed by ISH using a *loxl2b*-specific probe on spinal cord sections of *Tg(-14.8gata4:EGFP)* animals (Figure S5B). To further examine the relationship between Gata4 and *loxl2b*, we generated a transgenic zebrafish line expressing *gata4* downstream of the heat shock-inducible *hsp70l* promoter. Induction of *gata4* overexpression was associated with reduced *loxl2b* expression after SCI, consistent with Gata4 negatively regulating *loxl2b* expression *in vivo* (Figures S5D–S5F). Together, these findings indicate that loss of Gata4 induces a broad ECM-remodeling transcriptional program in ERGs. The enrichment of the ECM-receptor interaction pathway suggests altered cell-matrix signaling, while the upregulation of *loxl2b*, a known mediator of collagen cross-linking and fibrosis,[35,36] together with its repression by Gata4 overexpression, identifies *loxl2b* as a downstream target of Gata4. These observations suggest that loss of Gata4 may promote pathological ECM remodeling during spinal cord regeneration.

Gata4-mutant ERGs are molecularly distinct from mouse reactive astrocytes and exhibit features of mouse fibroblast programs

The enrichment of collagen and other ECM-related genes in *gata4*$^{wcm6/wcm6}$ ERGs led us to speculate that these cells may acquire a transcriptional program similar to mouse reactive astrocytes. To test this, we first generated a list of zebrafish genes enriched in *gata4*$^{wcm6/wcm6}$ versus wild-type ERGs at 2 wpi and mapped them to their mouse orthologs. This ortholog gene set was then used to examine expression in a previously published mouse reactive-astrocyte dataset[37] (Figure S6A). Comparison of differentially expressed genes (DEGs) between *gata4*$^{wcm6/wcm6}$ versus wild-type ERGs and those generated from mouse reactive versus homeostatic astrocytes revealed minimal correlation in fold-change values. GSEA of concordant and non-concordant genes did not identify shared pathways (Figures S6B and S6C; Tables S3 and S4). In addition, *Loxl2, Col18a1,* and *Col27a1*, three genes we confirmed were upregulated in *gata4*$^{wcm6/wcm6}$ versus wild-type ERGs (Figures 3G–3I), were only sparsely expressed in mouse reactive astrocytes, suggesting low overall transcript abundance (Figures S6D–S6F). These findings suggest that *gata4*$^{wcm6/wcm6}$ ERGs may engage molecular programs distinct from those of mammalian reactive astrocytes, possibly reflecting fundamental differences between zebrafish glia and mammalian astrocytes or a limited capacity for zebrafish ERGs to adopt a reactive astrocyte-like state following Gata4 loss-of-function.

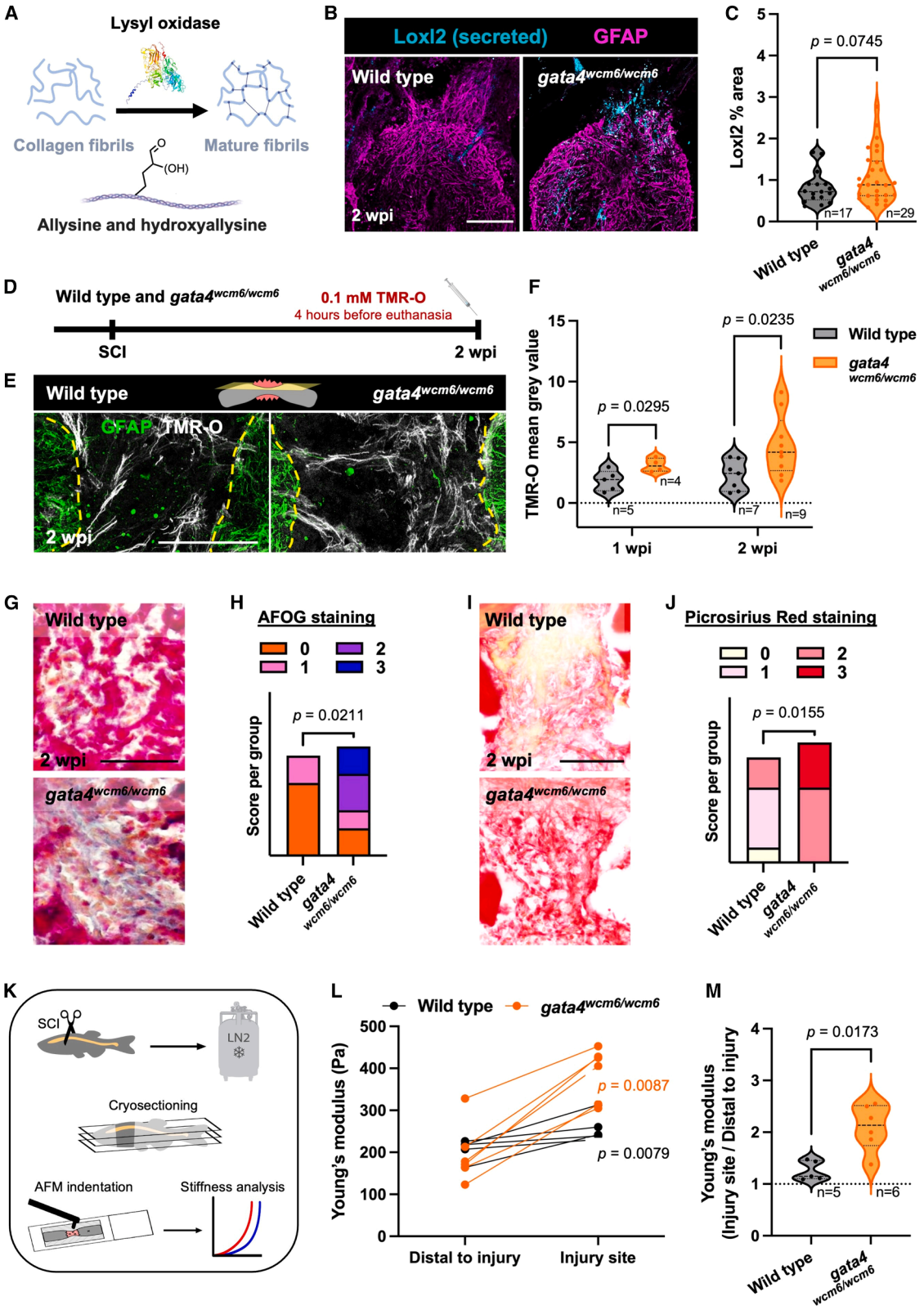
Given the strong induction of *loxl2b*, *col18a1a,* and *vimentin*, genes commonly expressed in fibroblasts,[38–43] in *gata4*$^{wcm6/wcm6}$ ERGs (Figures 3F–3I), we asked whether *gata4*-mutant ERGs may engage molecular programs similar to those of mouse scar-forming fibroblasts, rather than a reactive astrocyte-like phenotype following SCI. We mapped DEGs from *gata4*$^{wcm6/wcm6}$ versus wild-type ERGs to their mouse orthologs and assessed their expression in mouse fibroblasts after SCI compared with uninjured fibroblasts. For this analysis, we reprocessed a previously published single-cell RNA-sequencing dataset,[44] re-annotating cell types to recover fibroblast populations at 0 and 2 wpi (Figure S7A). Differential expression and pathway analyses revealed extensive transcriptional remodeling of mouse fibroblasts after injury (Figure S7B). *Loxl2b*, *Col18a1*, *Col27a1,* and additional genes including *Vim*, *Fn1*, *Col1a1,* and *Col16a1*, all robustly induced in *gata4*$^{wcm6/wcm6}$ ERGs, were significantly upregulated in post-injury mouse fibroblasts (Figures S7D–S7J; Table S5). Moreover, post-injury mouse fibroblasts showed strong enrichment of immune-related pathways and upregulation of ECM-receptor interaction and collagen biosynthesis pathways (Figure S7C; Table S6). These same ECM-related pathways were among the most enriched in *gata4*$^{wcm6/wcm6}$ ERGs (Figure 3D; Table S2). Consistent with these transcriptional analyses, immunofluorescence in the adult mouse spinal cord using an antibody[45] that specifically recognizes the secreted form of LOXL2 revealed its presence at the lesion site, within the fibrotic scar where fibronectin is also present, and in and around COL1A2-positive fibroblast-rich regions (Figures S7K and S7L).

Together, these results suggest that *gata4* loss-of-function in zebrafish is associated with increased production of ECM components in ERGs, with a potential minor contribution from other cell types, rather than a canonical reactive astrocyte response. This shift likely reflects a transition toward a fibrosis-like repair mode, highlighting a role for zebrafish Gata4 in constraining excessive matrix production during spinal cord regeneration.

Gata4 loss-of-function increases secreted Loxl2b levels, leading to spinal cord fibrosis

loxl2b, one of several zebrafish paralogs within the lysyl oxidase family, was among the most highly upregulated transcripts in

(E) Rank plot of ECM pathway genes by $\log_2$ fold change; inset highlights genes with the highest fold changes.
(F) Expression of *loxl2b, col27a1b, col18a1a, fn1a, vim, col1a1b,* and *col16a1* in wild-type and *gata4*$^{wcm6/wcm6}$ ERGs at 2 wpi.
(G–I) *In situ* hybridization and quantification of *loxl2b* (G), *col27a1b* (H), and *col18a1a* (I) in wild-type and *gata4*$^{wcm6/wcm6}$ spinal cords at 2 wpi. Dashed lines delineate spinal cord tissue. Scale bars, 100 μm (G–I).



(legend on next page)

gata4$^{wcm6/wcm6}$ ERGs compared to wild type after SCI. This protein catalyzes collagen cross-linking by converting lysine and hydroxylysine residues into reactive aldehydes (Lys^{Ald}) that form covalent bonds between collagen fibrils, creating a stable and rigid ECM (Figures 4A and S8A).[46] To confirm that *loxl2b* transcriptional signal corresponds to protein-level changes, we performed immunofluorescence using the same antibody recognizing the secreted mature form of LOXL2 used for the mouse spinal cord analysis (Figure S7L).[45] Although this antibody does not distinguish between the Loxl2a and Loxl2b zebrafish paralogs, our transcriptomic analysis did not detect upregulated expression of *loxl2a* in *gata4*$^{wcm6/wcm6}$ spinal cords, indicating that the immunoreactivity observed in mutants likely reflects Loxl2b. Immunofluorescence revealed a trend toward increased Loxl2 accumulation in and around the regenerating site of *gata4*$^{wcm6/wcm6}$ zebrafish compared to wild-type controls at 2 wpi, suggesting altered collagen remodeling in the absence of Gata4 (Figures 4B, 4C, and S5C). To assess collagen cross-linking, we used TMR-O, a fluorescent probe that binds Lys^{Ald} residues generated by lysyl oxidase enzymes on collagen that are actively undergoing cross-linking[47,48] (Figure S8A). TMR-O labeled injured but not uninjured spinal cords, whereas the non-binding TMR-NB control probe showed no signal (Figures S8B and S8C). TMR-O fluorescence was increased in *gata4*$^{wcm6/wcm6}$ lesions compared with wild type by ~70% at 1 wpi and ~108% at 2 wpi (Figures 4D–4F), indicating enhanced collagen cross-linking.

To correlate TMR-O signal with fibrotic tissue deposition, we performed Acid Fuchsin-Orange G (AFOG) staining, which labels fibrin and collagen, on spinal cord tissue sections at 2 wpi, when TMR-O reactivity was highest. AFOG staining revealed no differences between uninjured spinal cords from wild-type or *gata4*$^{wcm6/wcm6}$ zebrafish (Figure S9A). In contrast, injured *gata4*$^{wcm6/wcm6}$ spinal cords exhibited more extensive fibrosis, indicated by increased aniline blue staining than injured wild-type spinal cords (Figure 4G). To further assess collagen deposition, we performed Picrosirius Red staining to specifically highlight collagen fibers. Consistent with the AFOG results, uninjured spinal cords showed no detectable differences between genotypes (Figure S9C), whereas 2 wpi *gata4*$^{wcm6/wcm6}$ spinal cords displayed increased collagen accumulation relative to wild type (Figures 4I and S9D). Quantification of both AFOG and Picrosirius Red staining confirmed significantly elevated fibrosis in mutant animals (Figures 4H and 4J), indicating that *gata4* loss-of-function promotes excessive scar formation after SCI. To determine if the increased fibrosis in *gata4*$^{wcm6/wcm6}$ is accompanied by broader changes in ECM composition, particularly chondroitin sulfate proteoglycans (CSPGs)-associated ECM, we stained spinal cord tissue sections with Wisteria floribunda agglutinin (WFA, a lectin that binds α-galactose-containing glycans and labels glycoprotein- and glycan-rich ECM). WFA binding was broadly distributed throughout the spinal cord, consistent with previous reports in zebrafish.[49] We detected no significant difference, however, in WFA intensity between wild-type and *gata4*$^{wcm6/wcm6}$ animals at 2 wpi (Figures S9E and S9F). These findings suggest that the enhanced fibrosis observed in *gata4* mutants is not accompanied by broad changes in WFA-reactive, CSPG-associated ECM.

Prior studies have correlated ECM remodeling with changes in tissue stiffness and axon regeneration after SCI in both rodents and zebrafish.[16,50–52] We therefore performed atomic-force microscopy (AFM) at 2 wpi (Figures 4K and S8D), to assess tissue mechanical properties. As expected, lesion-proximal tissue displayed significantly increased stiffness compared to distal tissue in both *gata4*$^{wcm6/wcm6}$ and wild-type spinal cords (Figures 4L, S8E, and S8F).[52] There was no difference in tissue stiffness between uninjured spinal cord of wild-type and *gata4*$^{wcm6/wcm6}$ zebrafish (Figure S8G). Regions distal to the lesion site showed similar stiffness between genotypes (wild-type: 206.9 ± 24.9 Pa; *gata4*$^{wcm6/wcm6}$: 196.2 ± 70.7 Pa), whereas lesion sites were substantially stiffer in *gata4* mutants compared with wild-type animals (wild-type: 256.9 ± 33.2 Pa; *gata4*$^{wcm6/wcm6}$: 388.4 ± 62.7 Pa) (Figures 4L and 4M), consistent with increased fibrosis and collagen cross-linking. These findings show that Gata4 loss-of-function induces a pro-fibrotic state in the zebrafish spinal cord, with elevated Loxl2b, increased collagen cross-linking and changes in mechanical tissue properties. This fibrotic phenotype somewhat mirrors the fibrotic scarring observed in mouse SCI (Figure S9B).

Inhibition of Loxl2b rescues regeneration defects in *gata4*$^{wcm6/wcm6}$ mutants

To determine if the phenotype observed in *gata4*$^{wcm6/wcm6}$ zebrafish could be ameliorated by blocking the elevated Loxl2b

Figure 4. Gata4 loss-of-function promotes scarring and increases spinal cord stiffness

(A) Lysyl oxidase reaction. Oxidation of lysine and hydroxylysine residues generates reactive aldehydes (LysAld) that mediate collagen cross-linking.

(B and C) Loxl2 immunofluorescence in wild-type and *gata4*$^{wcm6/wcm6}$ spinal cords at 2 weeks post-injury (wpi) (B) and quantification in (C). One side of the injury site is shown.

(D) TMR-O administration protocol.

(E and F) TMR-O fluorescence (gray) and GFAP (green) in *gata4*$^{wcm6/wcm6}$ and wild type spinal cords (E) and TMR-O quantification at 1 and 2 wpi (F).

(G and H) AFOG staining (G) and semiquantitative assessment of collagen deposition (H). Scores: 0, no detectable collagen; 1, low; 2, moderate; 3, high. n = 11 wild type, n = 12 *gata4*$^{wcm6/wcm6}$.

(I and J) Picrosirius Red staining (I) and semiquantitative assessment of collagen deposition (J) using the same scoring criteria as in (H). n = 7 wild-type, n = 8 *gata4*$^{wcm6/wcm6}$.

(K) Atomic force microscopy pipeline.

(L) Apparent Young's moduli at the lesion and distal regions of wild-type and *gata4*$^{wcm6/wcm6}$ spinal cords at 2 wpi. Lines connect measurements from the same animal.

(M) Ratio of lesion to distal Young's modulus.

Violin plots show the data distribution; dashed lines denote medians and dotted lines denote the 25th and 75th percentiles. Each dot in (C, F, and M) represents one animal. Scale bars, 50 μm (B, G, and I) and 100 μm (E). Mann-Whitney test (L and M); Welch's t test (C and F); Fisher's exact test (H and J).

activity, we treated animals with β-aminopropionitrile (BAPN). This potent and irreversible inhibitor of lysyl oxidases has been extensively characterized and used across multiple model organisms, including zebrafish.[53–55] We opted for broad pharmacological inhibition rather than cell-type-specific genetic ablation to counteract potential contributions from Loxl2b secreted by non-glial cell types at the injury site (Figures 1A and S1F–S1H). *gata4*$^{wcm6/wcm6}$ animals were injured and incubated with BAPN for two weeks (Figure 5A). BAPN administration reversed the increased collagen deposition observed in and around the lesion of *gata4*$^{wcm6/wcm6}$ animals, reducing it to levels comparable to wild type, as assessed by AFOG staining (Figures 5B and 5C). We also analyzed 2 wpi spinal cords from zebrafish treated with BAPN and injected with the TMR-O probe. BAPN treatment reduced TMR-O labeling in *gata4*$^{wcm6/wcm6}$ lesions to levels comparable to those of regenerating wild-type animals (Figures 5D and 5E). We assessed functional recovery following injury by subjecting wild-type, *gata4*$^{wcm6/wcm6}$, and BAPN-treated *gata4*$^{wcm6/wcm6}$ animals to swim tests. Uninjured animals showed no differences in swim capacity across groups (Figure 5F). Following SCI, *gata4*$^{wcm6/wcm6}$ animals consistently exhibited a trend toward reduced swim recovery compared with wild-type animals, although this difference did not reach statistical significance by Mann-Whitney test, likely due to inter-individual variability. Notably, BAPN treatment restored swim performance in *gata4*$^{wcm6/wcm6}$ animals to levels similar to wild type, offsetting the reduced recovery observed in non-BAPN-treated mutants (Figure 5G). These results correlated with histological analyses of spinal cord tissue, where BAPN-untreated *gata4*$^{wcm6/wcm6}$ animals showed a ∼38% and ∼47% reduction in glial and axon bridging, respectively, compared with BAPN-untreated wild types. Remarkably, BAPN treatment completely rescued these *gata4*$^{wcm6/wcm6}$ defects, restoring glial and axon bridge formation to wild-type levels (Figures 5H–5J). Importantly, BAPN treatment did not significantly impair swim recovery, glial bridging, or axonal bridging in wild-type animals undergoing SCI, indicating that reducing collagen cross-linking alone is not sufficient to compromise regeneration in an otherwise permissive environment (Figure S10). Together, these results indicate that BAPN treatment rescues excessive collagen deposition, glial and axonal bridging and, at least partially, the functional recovery defect in *gata4*$^{wcm6/wcm6}$ animals following SCI.

Hif-1α contributes to the post-SCI induction of *gata4* via an upstream *cis*-regulatory region

To identify signals upregulating *gata4* post-SCI, we screened injury-associated cues in *Tg(-14.8gata4:EGFP; gfap-H2A:mCherry)* larvae, whose rapid regeneration and optical transparency enable longitudinal *in vivo* visualization of glia and *gata4*:EGFP activity.[56,57] We considered hypoxia and reactive oxygen species (ROS) production as potential injury-associated regulators of *gata4* (Figure 6A). Uninjured larvae at 2 days post fertilization (dpf) were treated with dimethyloxalylglycine (DMOG), which stabilizes the oxygen-sensitive transcription factor hypoxia-inducible factor 1A (HIF-1α) and activates hypoxic signaling[58,59]; phenylhydrazine (PHZ), which induces anemia[60,61]; or hydrogen peroxide (H_2O_2), which induces ROS generation[62] (Figure 6B). Using uninjured larvae allowed us to identify candidate upstream activators of *gata4* independently of injury. Among these treatments, constant exposure to DMOG induced robust *gata4:EGFP* expression in spinal cord ERGs at 5 dpf, whereas PHZ and H_2O_2 treatment produced no detectable phenotype (Figures 6C and 6D; Movie S1). This indicates that hypoxic signaling is sufficient to, at least partially, activate glial *gata4* transcription in the absence of injury.

We next combined DMOG treatment with spinal cord transection to determine whether Hif-1α stabilization enhances *gata4:EGFP* activation after injury. Larvae injured at 3 dpf were continuously exposed to DMOG and imaged at 6 dpf (3 dpi) (Figure 6E). DMOG increased EGFP signal approximately 2.6-fold at the lesion site, with a similar increase rostral and caudal to the lesion, indicating that DMOG enhances *gata4* expression beyond injury-induced levels (Figures 6F and 6G; nc in F indicates the notochord, previously shown to express *gata4* during development[30]). To test whether Hif-1α is not only sufficient but also required for *gata4* activation, injured larvae were treated with PX-478, a small-molecule inhibitor that suppresses Hif-1α protein accumulation and transcriptional activity,[63] and analyzed at 3 dpi (Figure 6H). PX-478 reduced *gata4:EGFP* reporter signal at the lesion site by ∼17% compared to vehicle-treated controls (Figures 6I and 6J). Together, these findings indicate that Hif-1α signaling contributes to injury-induced *gata4* expression.

To identify *cis*-acting regulatory DNA sequences driving localized *gata4* activation after SCI, we analyzed spinal cord chromatin accessibility datasets we previously generated[14] focusing on the −14.8 kb upstream regulatory region of the *Tg(-14.8gata4:EGFP)* reporter line. This analysis identified two regions with increased chromatin accessibility at 1 wpi compared with sham-injured controls, in which skin and muscle were cut but the spinal cord remained intact (dashed lines, Figure 6K). One ∼620 bp dynamically accessible sequence, *gata4EN1*, was located about −2.7 kb relative to the *gata4* transcriptional start site (TSS), while a second one, *gata4EN2,* was ∼680 bp in length and located −7.3 kb upstream of the TSS. To test whether these regions can direct injury-induced gene expression after SCI, we placed them upstream of the normally silent minimal promoter *c-fos,* and an EGFP reporter gene. Constructs were injected into fertilized zebrafish eggs, which underwent spinal cord transection injury at 3 dpf, followed by EGFP signal assessment at the lesion site by *in vivo* imaging at 4, 5, and 6 dpf (Figure 6L). We did not detect spinal cord fluorescence in uninjured *gata4EN1-c-fos:EGFP* or *gata4EN2-c-fos:EGFP* animals, nor in animals carrying a *c-fos:EGFP* control construct. Following SCI, *gata4EN2-c-fos:EGFP* and *c-fos:EGFP* control animals showed no EGFP signal, whereas *gata4EN1* directed EGFP expression at SCI sites (Figure 6M). This pattern of expression closely mirrored that observed in *Tg(-14.8gata4:EGFP)* larvae (Figures 6F and 6I, control panels). Cells expressing EGFP in the spinal cord were identified as glial cells using colocalization with the glial marker GFAP (Figure S11A).

To further understand *gata4* regulation post-SCI, we performed FIMO motif scanning across the −14.8 kb *gata4* upstream region, selecting a broad range of TF families implicated in regeneration, stress/inflammation, chromatin remodeling, mechanical response, development, and pioneer TF activity. This analysis identified predicted binding sites for multiple TF families,

CellPress
OPEN ACCESS

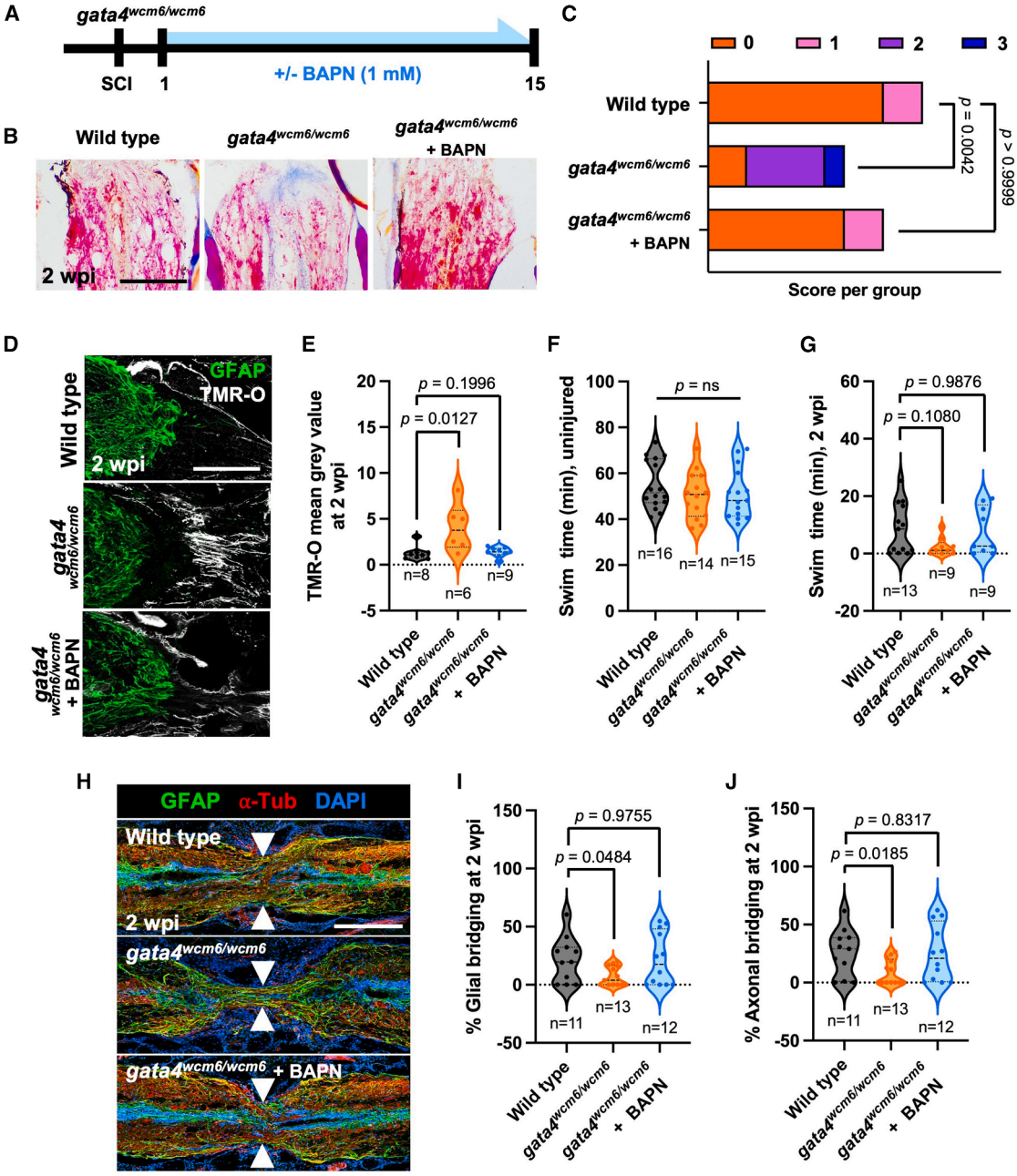


Figure 5. Pharmacological inhibition of Loxl2b reduces fibrosis and restores tissue bridging and function in *gata4*$^{wcm6/wcm6}$ spinal cords

(A) BAPN administration protocol.

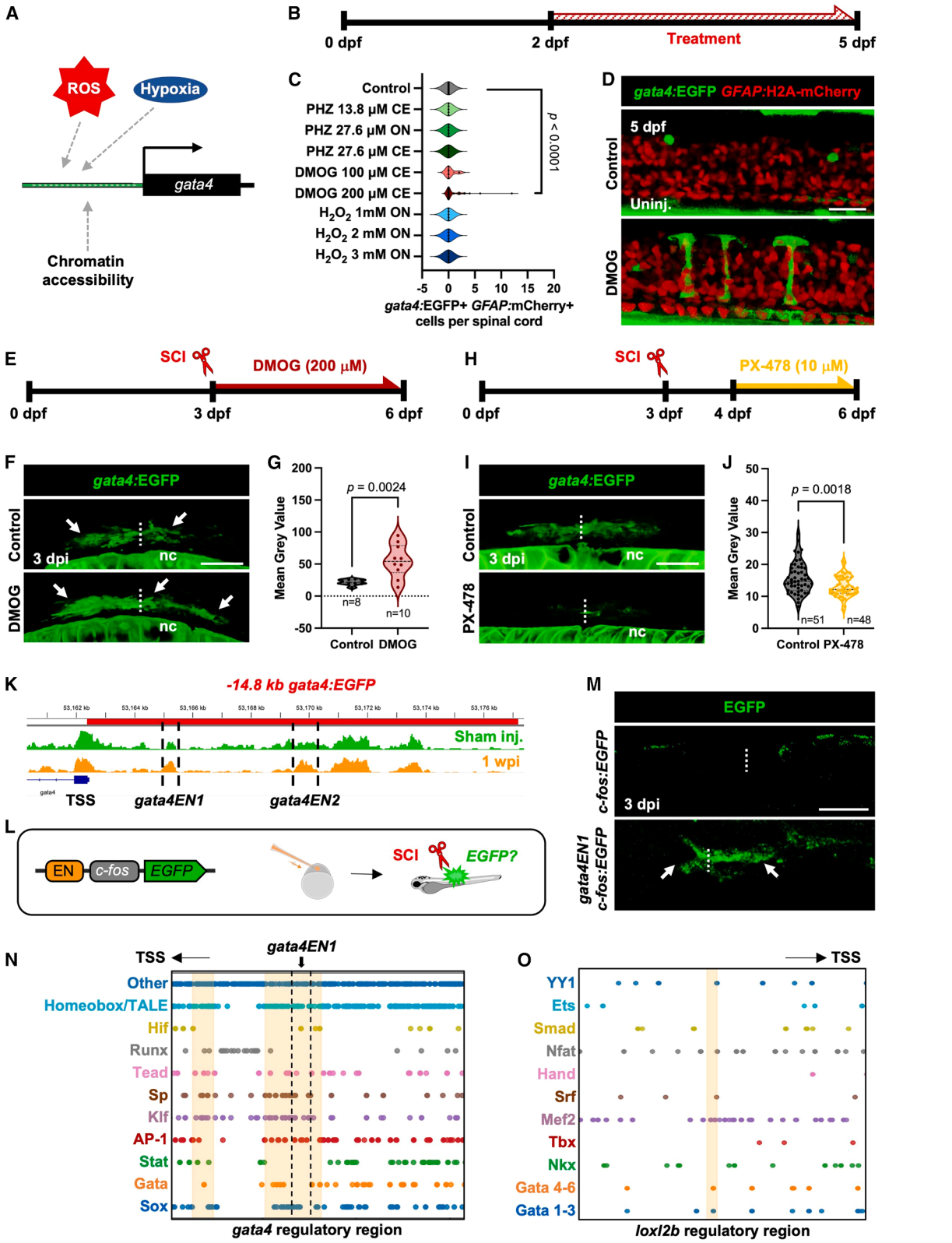
(B and C) AFOG staining (B) and semiquantitative assessment of collagen deposition (C) in wild-type, *gata4*$^{wcm6/wcm6}$, and BAPN-treated *gata4*$^{wcm6/wcm6}$ spinal cords at 2 weeks post-injury (wpi). Scores: 0: no detectable collagen; 1: low; 2: moderate; 3: high. n = 11 wild type, n = 7 *gata4*$^{wcm6/wcm6}$ and n = 9 *gata4*$^{wcm6/wcm6}$ + BAPN.

(D and E) TMR-O fluorescence (gray) and GFAP (green) in wild-type, *gata4*$^{wcm6/wcm6}$, and BAPN-treated *gata4*$^{wcm6/wcm6}$ spinal cords at 2 wpi (D) and TMR-O quantification (E).

(F and G) Endurance swim capacity in uninjured (F) and 2 wpi (G) wild-type, *gata4*$^{wcm6/wcm6}$, and BAPN-treated *gata4*$^{wcm6/wcm6}$ zebrafish.

(H–J) GFAP (green) and acetylated α-tubulin (red) staining in longitudinal sections at 2 wpi (H) and quantification of glial (I) and axonal (J) bridging in wild-type, *gata4*$^{wcm6/wcm6}$, and BAPN-treated *gata4*$^{wcm6/wcm6}$ spinal cords. Arrows indicate tissue bridges.

Violin plots show the data distribution; dashed lines denote medians and dotted lines denote the 25th and 75th percentiles. Each dot in (E–G, I, and J) represents one animal. Scale bars, 100 μm (B and D) and 150 μm (H). Fisher's exact test (C); Mann-Whitney test (E–G, I, and J).



(legend on next page)

including Homeobox/TALE, Hif, Runx, Tead, Sp, Klf, AP-1, Stat, Gata, and Sox (Figures 6N and S11B; Tables S7 and S8). Two prominent motif-dense regions were identified at ~0.5–1.1 kb and ~2–3 kb upstream of the TSS, the latter overlapping with *gata4EN1*. Hif-1α, Klf, and Sp motifs were among the most significant (Figure 6N).[64] Because Klf and Sp factors physically and functionally interact with Gata4 and can be regulated by Hif-1α,[65,66] Hif-1α may activate *gata4* directly through its upstream regulatory region or indirectly through Klf and Sp, with both mechanisms potentially contributing.

Given that *loxl2b* was identified as a downstream target of Gata4, we analyzed its upstream regulatory region by FIMO motif scanning. The −5 kb *loxl2b* upstream sequence contained discrete motif-dense regions, including a prominent cluster ~3.8 kb upstream of the TSS containing Gata, Nkx, Mef2, Srf, and Ets motifs (Figures 6O and S11C; Tables S9 and S10). Multiple GATA motifs within this region support potential direct regulation of *loxl2b* by Gata4, possibly in co-operation with Mef2, which has been previously reported to co-bind with Gata4 to regulate gene expression.[67] Together, these findings support a model in which Gata4 influences ECM remodeling through transcriptional regulation of *loxl2b*.

Hif-1α signaling elicits distinct Gata4 and Loxl2 responses in zebrafish and human glial cells

To further investigate the Hif-1α-Gata4 regulatory relationship, we performed complementary *in vitro* analyses. Adult zebrafish spinal cords were dissociated to establish glia-enriched cultures (Figures S12A and S12B), which were treated with DMOG to activate Hif-1α signaling. Although the Hif-1α antibody we tested did not reliably detect zebrafish Hif-1α protein, precluding direct quantification of pathway activation, DMOG treatment significantly increased *gata4* expression to approximately 6.2-fold relative to control after 2 days of treatment ($p = 0.0179$; Figure S12C). In contrast, *loxl2b* expression was not significantly altered, suggesting that Hif-1α-mediated induction of *gata4* alone is insufficient to repress *loxl2b in vitro* and that additional injury-associated signals or cell-cell interactions are required *in vivo*.

To determine whether this regulatory relationship is conserved in mammalian cells, we next treated human iPSC-derived astrocytes with DMOG (Figures S12D–S12G). Consistent with activation of hypoxia-responsive signaling, DMOG treatment significantly increased nuclear HIF-1α levels (Figures S12E and S12F). Unlike zebrafish spinal cord cultures, however, HIF-1α stabilization did not induce *GATA4* expression in human astrocytes. Instead, DMOG treatment resulted in a 2.9-fold decrease in *GATA4* expression and a 3.2-fold increase in *LOXL2* expression (Figure S12G). These findings support a model in which Hif-1α functions upstream of *gata4* in zebrafish glial cells but indicate that the downstream transcriptional response to HIF-1α differs in human astrocytes. Together, these results provide independent *in vitro* support for the Hif-1α-Gata4 regulatory axis identified *in vivo* and suggest that hypoxia-responsive signaling may be coupled to distinct transcriptional programs in regenerative and non-regenerative glial cells.

DISCUSSION

Our study identifies Gata4 as a regulator that preserves ERG identity and regenerative competence following SCI in zebrafish. Loss of Gata4 promotes a fibroblast-like, ECM-associated transcriptional program and pathological matrix remodeling resulting in fibrosis and altered tissue mechanics. The absence of changes in CSPG levels in *gata4* mutants suggests that Gata4 selectively restrains fibrotic ECM remodeling rather than broadly regulating injury-associated ECM.

The relationship between tissue mechanics and regeneration remains complex and context-dependent, with studies reporting both tissue softening and stiffening following SCI depending on the model, time point, and region analyzed.[16,50–52] Although *gata4* mutants exhibited increased lesion stiffness and impaired regeneration, BAPN treatment in wild-type animals, which reduces collagen cross-linking and is predicted to decrease tissue stiffness, did not significantly alter glial or axon bridging or functional recovery. Together, these findings suggest that suppression of fibrotic remodeling, rather than tissue stiffness per se,

Figure 6. Hif-1α contributes to injury-induced *gata4* expression through an upstream cis-regulatory region

(A) Selected injury-associated signals tested as possible inducers of *gata4*.
(B) Experimental design for treatments of uninjured larvae.
(C) Number of *gata4*:EGFP$^+$ glial cells in *Tg(-14.8gata4:EGFP; gfap:H2A-mCherry)* larvae treated with phenylhydrazine (PHZ), dimethyloxalylglycine (DMOG), or hydrogen peroxide (H_2O_2). ON, overnight; CE, constant exposure.
(D) *Tg(-14.8gata4:EGFP; gfap:H2A-mCherry)* larval spinal cords after DMOG exposure. GFAP labels glial nuclei.
(E) Experimental design for DMOG treatment following spinal cord injury (SCI).
(F and G) *gata4:*EGFP expression and quantification at 3 days post-injury (dpi) with or without DMOG treatment.
(H) Experimental design for PX-478 treatment following SCI.
(I and J) *gata4:*EGFP expression and quantification at 3 dpi with and without PX-478 treatment.
(K) ATAC-seq tracks showing two regions of increased chromatin accessibility (*gata4EN1* and *gata4EN2*) within the *-14.8gata4* upstream regulatory region at 1 week post injury.
(L) Strategy for *in vivo gata4EN1* and *gata4EN2* enhancer analysis.
(M) Injury-induced expression driven by *gata4EN1* at 3 dpi.
(N and O) FIMO motif analysis of the *gata4* (N) and *loxl2b* (O) upstream regulatory regions, showing predicted TF-binding sites by family and position relative to the transcription start site. Shading indicates motif-dense regions identified using gene-specific clustering criteria (see STAR Methods). The *loxl2b* region includes predicted GATA-binding sites. Complete upstream regulatory regions are shown in Figure S11.
nc, notochord (F and I), previously shown to express *-14.8gata4:*EGFP during development. Violin plots show the data distribution; dashed lines denote medians and dotted lines denote the 25th and 75th percentiles. Each dot in (C, G, and J) represents one larva. Scale bars, 20 μm (D), 100 μm (F and I). Mann-Whitney test (C); Welch's *t* test (G and J).

is important for regenerative repair and position Gata4 as a transcriptional safeguard against maladaptive matrix remodeling.

The ECM components that accumulate in Gata4-deficient lesions are similar to those that dominate the mammalian fibrotic scar.[1] Loxl2b emerges as an important downstream effector of Gata4, with increased expression and activity in Gata4-deficient ERGs driving enhanced collagen cross-linking and matrix stabilization. BAPN-mediated inhibition of lysyl oxidases reduced fibrosis and restored glial and axonal bridge in Gata4-deficient zebrafish, supporting a role for Gata4-dependent control of collagen cross-linking in regeneration. Given that GATA4 also suppresses fibrogenic programs in heart and liver repair in mammals,[24,68] our findings point to a conserved anti-fibrotic role for this factor across regenerative contexts and species. Persistent reduction in synaptic vesicle abundance and defects in spinal curvature in *gata4* mutants further suggest that abnormal ECM remodeling may have consequences for spinal cord architecture and circuit reconstruction beyond the initial regenerative period.

Our findings also connect injury-responsive Hif-1α signaling to *gata4* activation. Stabilization of Hif-1α with DMOG is sufficient to induce *gata4* expression in *uninjured* glia, suggesting that injury-associated hypoxia may contribute to *gata4* induction. The *gata4* upstream regulatory region contains clusters of Hif-1α, Klf, Sp, and other TF motifs, consistent with integration of multiple injury-responsive signals. Because Klf and Sp factors can also be modulated by Hif-1α,[65,66] both direct and indirect mechanisms may contribute to Hif-1α-mediated *gata4* regulation.

The failure of PHZ-induced anemia to activate *gata4*, together with reduced *gata4* expression following PX-478 treatment, suggests that localized or sustained Hif-1α activity, rather than systemic oxygen deprivation, contributes to injury-induced *gata4* expression. Unlike DMOG, which directly stabilizes Hif-1α, PHZ induces systemic hypoxia through hemolytic anemia and may not generate sufficiently localized or sustained Hif-1α activation in spinal cord glia to induce the pro-regenerative transcriptional program. However, because tissue-level hypoxia was not directly measured after PHZ treatment, this interpretation remains tentative.

The downstream consequences of HIF-1α activation may differ in zebrafish and mammals. Whereas DMOG treatment increased *gata4* expression in zebrafish glia-enriched cultures, it reduced *GATA4* expression and increased *LOXL2* expression in human astrocytes. These findings are consistent with recent evidence that regenerative and non-regenerative vertebrates differ in their oxygen-sensing capacity and HIF-1α-dependent responses, with regenerative species exhibiting more sustained HIF-1α activity across a broad range of oxygen conditions.[69] Our results suggest that these species differences may also extend to transcriptional programs downstream of HIF-1α signaling.

More broadly, our findings indicate that zebrafish glial cells do more than provide a passive structural bridge during spinal cord regeneration. Instead, they actively constrain fibrotic matrix remodeling and maintain an environment permissive for axonal regrowth. Translationally, our data suggest that enhancing GATA4 activity or inhibiting collagen cross-linking enzymes such as LOXL2, through agents such as BAPN, could mitigate fibrosis and promote repair in the injured mammalian CNS. Notably, a 2001 study reported that BAPN-mediated lysyl oxidase inhibition significantly improved motor recovery after SCI in mice[70] but the underlying cellular mechanisms, particularly those related to axon regeneration, remain largely unexplored. Furthermore, we consider the zebrafish *gata4*$^{wcm6/wcm6}$ model to be a valuable platform to test anti-fibrotic compounds and uncover new regulators of scar formation.

Together, our findings establish GATA4 as a transcriptional node linking injury-sensing, glial cell state, and ECM dynamics. More broadly, this work illustrates how differentiated cells actively stabilize tissue architecture after injury by suppressing pathological matrix stiffening and fibrotic scar formation, revealing an organizing principle that may extend across regenerative neural tissues and other regenerative contexts.

Limitations of the study

While our findings identify Gata4 as a regulator of ECM remodeling during spinal cord regeneration, several limitations remain. DMOG also inhibits certain histone demethylases, so its effects on zebrafish *gata4* activation may not be exclusively Hif-1α-mediated. Future chromatin-based approaches will be required to determine whether Gata4 directly regulates *loxl2b* expression, and to dissect direct versus indirect effects of Hif-1α on *gata4* regulatory regions. The *gata4*$^{wcm6/wcm6}$ mutation is global, limiting assignment of cell-type-specific roles. Although tissue bridging recovers in mutants, persistent swimming deficits may reflect motor or circuit-level impairments not captured by our endurance assay. Finally, cross-species comparisons were performed using datasets generated under different injury paradigms (transection vs. crush) and sequencing modalities (single-nucleus vs. single-cell RNA-seq), which may influence specific aspects of the comparison.

RESOURCE AVAILABILITY

Lead contact

Further information and requests for resources and reagents should be directed to and will be fulfilled by the Lead Contact: Valentina Cigliola (valentina.cigliola@vanderbilt.edu).

Materials availability

All plasmids, protocols, and zebrafish transgenic lines in this study are available upon request.

Data and code availability

- Single-nucleus RNA-sequencing data generated in this study have been deposited in the Gene Expression Omnibus (GEO) under the accession number GSE316679.
- Custom Python codes used for *in situ* hybridization quantification and motif analyses have been deposited at Zenodo (https://doi.org/10.5281/zenodo.21926882; https://doi.org/10.5281/zenodo.21926901; https://doi.org/10.5281/zenodo.21926910).
- Any additional data reported in this paper will be shared by the lead contact upon request.

ACKNOWLEDGMENTS

We thank Ken Poss for supporting preliminary studies on Gata4 in his laboratory. We are especially grateful to Chris V.E. Wright (Vanderbilt Program in

Developmental Biology) for insightful and in-depth discussions and comments on the manuscript. Members of the Cigliola laboratory provided valuable feedback and discussion throughout the project and on the manuscript. We also thank Isabel Spann, Guillaume Dupuy, and Cory Guthrie for zebrafish care, and Todd Evans for sharing the *gata4*$^{wcm6/wcm6}$ zebrafish line. We are grateful to Dimitry Koktysh at the Vanderbilt Institute of Nanoscale Science and Engineering for assistance with atomic force microscopy experiments, Agnès Loubat at the Flow Cytometry Platform of the Institute of Biology Valrose for support with single-nucleus RNA-sequencing library preparation, Spencer Dunn for computational tool development, and Oleg Kovtun at the Vanderbilt Cell Imaging Shared Resource for image analysis support. This work was supported by research funding from Vanderbilt University and the Vanderbilt Brain Institute (to V.C.), the National Institutes of Health (R35GM165955 to V.C. and T32GM149363 to P.E.P.), the French National Research Agency (ANR-22-CPJ1-0045-01 to V.C.), the LABEX SIGNALIFE program (ANR-11-LABX-0028-01 to V.C.), the IDEX UCA Jedi program (ANR-15-IDEX-01 to V.C.). The graphical abstract was created with BioRender.com.

AUTHOR CONTRIBUTIONS

Conceptualization: N.N., V.L.F., and V.C.; methodology: N.N., V.L.F., A.K., P.E.P., H.K., M.P.S., E.A.A.B., and V.C.; formal analysis: N.N., V.L.F., A.K., P.E.P., H.K., and V.C.; investigation: N.N., V.L.F., A.K., P.E.P., H.K., and V.C.; writing – original draft: V.C.; review and editing: all authors; resources and funding acquisition: V.C.; supervision: E.S.L., E.A.A.B., and V.C.

DECLARATION OF INTERESTS

The authors declare no competing interests.

STAR★METHODS

Detailed methods are provided in the online version of this paper and include the following:

- KEY RESOURCES TABLE
- EXPERIMENTAL MODEL AND STUDY PARTICIPANT DETAILS
  - Zebrafish
  - Generation of *hsp70l:gata4-P2A-EGFP* zebrafish
- METHOD DETAILS
  - Spinal cord injury
  - Immunofluorescence
  - *In situ* hybridization
  - AFOG, picrosirius and WFA staining
  - EdU labeling
  - Biocytin axon tracing
  - Drug and probe treatments
  - iPSC maintenance
  - iPSC differentiation into astrocytes
  - Zebrafish spinal cord cell culture
  - Quantitative real time PCR
  - Swim assays
  - Atomic force microscopy
  - Body curvature analysis
  - Single-nucleus RNA sequencing
  - Single-nucleus RNA sequencing analysis
  - Motif analyses
- QUANTIFICATION AND STATISTICAL ANALYSIS
  - Tissue bridge quantification
  - Loxl2 immunostaining quantification
  - Mean gray value analysis
  - Quantification of Syt2a+ axons
  - Colocalization analyses
  - *In situ* hybridization quantification
  - AFOG and Picrosirius Red staining quantification
  - Statistical analysis

SUPPLEMENTAL INFORMATION

Supplemental information can be found online at https://doi.org/10.1016/j.celrep.2026.118050.

Received: February 2, 2026
Revised: July 8, 2026
Accepted: September 7, 2026

REFERENCES

1. Bradbury, E.J., and Burnside, E.R. (2019). Moving beyond the glial scar for spinal cord repair. Nat. Commun. *10*, 3879. https://doi.org/10.1038/s41467-019-11707-7.
2. Tran, A.P., Warren, P.M., and Silver, J. (2018). The Biology of Regeneration Failure and Success After Spinal Cord Injury. Physiol. Rev. *98*, 881–917. https://doi.org/10.1152/physrev.00017.2017.
3. Soderblom, C., Luo, X., Blumenthal, E., Bray, E., Lyapichev, K., Ramos, J., Krishnan, V., Lai-Hsu, C., Park, K.K., Tsoulfas, P., and Lee, J.K. (2013). Perivascular fibroblasts form the fibrotic scar after contusive spinal cord injury. J. Neurosci. *33*, 13882–13887. https://doi.org/10.1523/JNEUROSCI.2524-13.2013.
4. Goritz, C., Dias, D.O., Tomilin, N., Barbacid, M., Shupliakov, O., and Frisen, J. (2011). A pericyte origin of spinal cord scar tissue. Science *333*, 238–242. https://doi.org/10.1126/science.1203165.
5. Dias, D.O., Kim, H., Holl, D., Werne Solnestam, B., Lundeberg, J., Carlen, M., Goritz, C., and Frisen, J. (2018). Reducing Pericyte-Derived Scarring Promotes Recovery after Spinal Cord Injury. Cell *173*, 153–165.e22. https://doi.org/10.1016/j.cell.2018.02.004.
6. Wanner, I.B., Anderson, M.A., Song, B., Levine, J., Fernandez, A., Gray-Thompson, Z., Ao, Y., and Sofroniew, M.V. (2013). Glial scar borders are formed by newly proliferated, elongated astrocytes that interact to corral inflammatory and fibrotic cells via STAT3-dependent mechanisms after spinal cord injury. J. Neurosci. *33*, 12870–12886. https://doi.org/10.1523/JNEUROSCI.2121-13.2013.
7. Sofroniew, M.V. (2009). Molecular dissection of reactive astrogliosis and glial scar formation. Trends Neurosci. *32*, 638–647. https://doi.org/10.1016/j.tins.2009.08.002.
8. Amlerova, Z., Chmelova, M., Anderova, M., and Vargova, L. (2024). Reactive gliosis in traumatic brain injury: a comprehensive review. Front. Cell. Neurosci. *18*, 1335849. https://doi.org/10.3389/fncel.2024.1335849.
9. Klapka, N., Hermanns, S., Straten, G., Masanneck, C., Duis, S., Hamers, F.P., Muller, D., Zuschratter, W., and Muller, H.W. (2005). Suppression of fibrous scarring in spinal cord injury of rat promotes long-distance regeneration of corticospinal tract axons, rescue of primary motoneurons in somatosensory cortex and significant functional recovery. Eur. J. Neurosci. *22*, 3047–3058. https://doi.org/10.1111/j.1460-9568.2005.04495.x.
10. Stichel, C.C., Hermanns, S., Luhmann, H.J., Lausberg, F., Niermann, H., D'Urso, D., Servos, G., Hartwig, H.G., and Muller, H.W. (1999). Inhibition of collagen IV deposition promotes regeneration of injured CNS axons. Eur. J. Neurosci. *11*, 632–646. https://doi.org/10.1046/j.1460-9568.1999.00466.x.
11. Becker, T., Wullimann, M.F., Becker, C.G., Bernhardt, R.R., and Schachner, M. (1997). Axonal regrowth after spinal cord transection in adult zebrafish. J. Comp. Neurol. *377*, 577–595. https://doi.org/10.1002/(sici)1096-9861(19970127)377:4<577::aid-cne8>3.0.co;2-#.
12. Reimer, M.M., Sorensen, I., Kuscha, V., Frank, R.E., Liu, C., Becker, C.G., and Becker, T. (2008). Motor neuron regeneration in adult zebrafish. J. Neurosci. *28*, 8510–8516. https://doi.org/10.1523/JNEUROSCI.1189-08.2008.
13. Mokalled, M.H., Patra, C., Dickson, A.L., Endo, T., Stainier, D.Y., and Poss, K.D. (2016). Injury-induced ctgfa directs glial bridging and spinal

cord regeneration in zebrafish. Science *354*, 630–634. https://doi.org/10.1126/science.aaf2679.

14. Cigliola, V., Shoffner, A., Lee, N., Ou, J., Gonzalez, T.J., Hoque, J., Becker, C.J., Han, Y., Shen, G., Faw, T.D., et al. (2023). Spinal cord repair is modulated by the neurogenic factor Hb-egf under direction of a regeneration-associated enhancer. Nat. Commun. *14*, 4857. https://doi.org/10.1038/s41467-023-40486-5.

15. Cigliola, V., Becker, C.J., and Poss, K.D. (2020). Building bridges, not walls: spinal cord regeneration in zebrafish. Dis. Model. Mech. *13*, dmm044131. https://doi.org/10.1242/dmm.044131.

16. Kolb, J., Tsata, V., John, N., Kim, K., Mockel, C., Rosso, G., Kurbel, V., Parmar, A., Sharma, G., Karandasheva, K., et al. (2023). Small leucine-rich proteoglycans inhibit CNS regeneration by modifying the structural and mechanical properties of the lesion environment. Nat. Commun. *14*, 6814. https://doi.org/10.1038/s41467-023-42339-7.

17. Wehner, D., Tsarouchas, T.M., Michael, A., Haase, C., Weidinger, G., Reimer, M.M., Becker, T., and Becker, C.G. (2017). Wnt signaling controls pro-regenerative Collagen XII in functional spinal cord regeneration in zebrafish. Nat. Commun. *8*, 126. https://doi.org/10.1038/s41467-017-00143-0.

18. Tsata, V., Mollmert, S., Schweitzer, C., Kolb, J., Mockel, C., Bohm, B., Rosso, G., Lange, C., Lesche, M., Hammer, J., et al. (2021). A switch in pdgfrb^{+} cell-derived ECM composition prevents inhibitory scarring and promotes axon regeneration in the zebrafish spinal cord. Dev. Cell *56*, 509–524.e9. https://doi.org/10.1016/j.devcel.2020.12.009.

19. John, N., Fleming, T., Kolb, J., Lyraki, O., Vasquez-Sepulveda, S., Parmar, A., Kim, K., Tarczewska, M., Gupta, P., Singh, K., et al. (2025). Biphasic inflammation control by fibroblasts enables spinal cord regeneration in zebrafish. Cell Rep. *44*, 116469. https://doi.org/10.1016/j.celrep.2025.116469.

20. Goldshmit, Y., Sztal, T.E., Jusuf, P.R., Hall, T.E., Nguyen-Chi, M., and Currie, P.D. (2012). Fgf-dependent glial cell bridges facilitate spinal cord regeneration in zebrafish. J. Neurosci. *32*, 7477–7492. https://doi.org/10.1523/JNEUROSCI.0758-12.2012.

21. Kikuchi, K., Holdway, J.E., Werdich, A.A., Anderson, R.M., Fang, Y., Egnaczyk, G.F., Evans, T., Macrae, C.A., Stainier, D.Y., and Poss, K.D. (2010). Primary contribution to zebrafish heart regeneration by gata4^{+} cardiomyocytes. Nature *464*, 601–605. https://doi.org/10.1038/nature08804.

22. Malek Mohammadi, M., Kattih, B., Grund, A., Froese, N., Korf-Klingebiel, M., Gigina, A., Schrameck, U., Rudat, C., Liang, Q., Kispert, A., et al. (2017). The transcription factor GATA4 promotes myocardial regeneration in neonatal mice. EMBO Mol. Med. *9*, 265–279. https://doi.org/10.15252/emmm.201606602.

23. Yu, W., Huang, X., Tian, X., Zhang, H., He, L., Wang, Y., Nie, Y., Hu, S., Lin, Z., Zhou, B., et al. (2016). GATA4 regulates Fgf16 to promote heart repair after injury. Development *143*, 936–949. https://doi.org/10.1242/dev.130971.

24. Arroyo, N., Villamayor, L., Diaz, I., Carmona, R., Ramos-Rodriguez, M., Munoz-Chapuli, R., Pasquali, L., Toscano, M.G., Martin, F., Cano, D.A., and Rojas, A. (2021). GATA4 induces liver fibrosis regression by deactivating hepatic stellate cells. JCI Insight *6*, e150059. https://doi.org/10.1172/jci.insight.150059.

25. Delgado, I., Carrasco, M., Cano, E., Carmona, R., Garcia-Carbonero, R., Marin-Gomez, L.M., Soria, B., Martin, F., Cano, D.A., Munoz-Chapuli, R., and Rojas, A. (2014). GATA4 loss in the septum transversum mesenchyme promotes liver fibrosis in mice. Hepatology *59*, 2358–2370. https://doi.org/10.1002/hep.27005.

26. Winkler, M., Staniczek, T., Kurschner, S.W., Schmid, C.D., Schonhaber, H., Cordero, J., Kessler, L., Mathes, A., Sticht, C., Nessling, M., et al. (2021). Endothelial GATA4 controls liver fibrosis and regeneration by preventing a pathogenic switch in angiocrine signaling. J. Hepatol. *74*, 380–393. https://doi.org/10.1016/j.jhep.2020.08.033.

27. Zhang, Z., Shayani, G., Xu, Y., Kim, A., Hong, Y., Feng, H., and Zhu, H. (2023). Induction of Senescence by Loss of Gata4 in Cardiac Fibroblasts. Cells *12*, 1652. https://doi.org/10.3390/cells12121652.

28. Agnihotri, S., Wolf, A., Picard, D., Hawkins, C., and Guha, A. (2009). GATA4 is a regulator of astrocyte cell proliferation and apoptosis in the human and murine central nervous system. Oncogene *28*, 3033–3046. https://doi.org/10.1038/onc.2009.159.

29. Agnihotri, S., Wolf, A., Munoz, D.M., Smith, C.J., Gajadhar, A., Restrepo, A., Clarke, I.D., Fuller, G.N., Kesari, S., Dirks, P.B., et al. (2011). A GATA4-regulated tumor suppressor network represses formation of malignant human astrocytomas. J. Exp. Med. *208*, 689–702. https://doi.org/10.1084/jem.20102099.

30. Heicklen-Klein, A., and Evans, T. (2004). T-box binding sites are required for activity of a cardiac GATA-4 enhancer. Dev. Biol. *267*, 490–504. https://doi.org/10.1016/j.ydbio.2003.09.042.

31. Zhou, L., McAdow, A.R., Yamada, H., Burris, B., Klatt Shaw, D., Oonk, K., Poss, K.D., and Mokalled, M.H. (2023). Progenitor-derived glia are required for spinal cord regeneration in zebrafish. Development *150*. https://doi.org/10.1242/dev.201162.

32. Klatt Shaw, D., Saraswathy, V.M., Zhou, L., McAdow, A.R., Burris, B., Butka, E., Morris, S.A., Dietmann, S., and Mokalled, M.H. (2021). Localized EMT reprograms glial progenitors to promote spinal cord repair. Dev. Cell *56*, 613–626.e7. https://doi.org/10.1016/j.devcel.2021.01.017.

33. Sam, J., Mercer, E.J., Torregroza, I., Banks, K.M., and Evans, T. (2020). Specificity, redundancy and dosage thresholds among gata4/5/6 genes during zebrafish cardiogenesis. Biol. Open *9*, bio053611. https://doi.org/10.1242/bio.053611.

34. Jensen, N.O., Burris, B., Zhou, L., Yamada, H., Reyes, C., Pincus, Z., and Mokalled, M.H. (2023). Functional trajectories during innate spinal cord repair. Front. Mol. Neurosci. *16*, 1155754. https://doi.org/10.3389/fnmol.2023.1155754.

35. Yang, J., Savvatis, K., Kang, J.S., Fan, P., Zhong, H., Schwartz, K., Barry, V., Mikels-Vigdal, A., Karpinski, S., Kornyeyev, D., et al. (2016). Targeting LOXL2 for cardiac interstitial fibrosis and heart failure treatment. Nat. Commun. *7*, 13710. https://doi.org/10.1038/ncomms13710.

36. Yamauchi, M., and Sricholpech, M. (2012). Lysine post-translational modifications of collagen. Essays Biochem. *52*, 113–133. https://doi.org/10.1042/bse0520113.

37. Li, C., Wu, Z., Zhou, L., Shao, J., Hu, X., Xu, W., Ren, Y., Zhu, X., Ge, W., Zhang, K., et al. (2022). Temporal and spatial cellular and molecular pathological alterations with single-cell resolution in the adult spinal cord after injury. Signal Transduction Targeted Ther. *7*, 65. https://doi.org/10.1038/s41392-022-00885-4.

38. Cheng, F., Shen, Y., Mohanasundaram, P., Lindstrom, M., Ivaska, J., Ny, T., and Eriksson, J.E. (2016). Vimentin coordinates fibroblast proliferation and keratinocyte differentiation in wound healing via TGF-beta-Slug signaling. Proc. Natl. Acad. Sci. USA *113*, E4320–E4327. https://doi.org/10.1073/pnas.1519197113.

39. Torres, S., Garcia-Palmero, I., Herrera, M., Bartolome, R.A., Pena, C., Fernandez-Acenero, M.J., Padilla, G., Pelaez-Garcia, A., Lopez-Lucendo, M., Rodriguez-Merlo, R., et al. (2015). LOXL2 Is Highly Expressed in Cancer-Associated Fibroblasts and Associates to Poor Colon Cancer Survival. Clin. Cancer Res. *21*, 4892–4902. https://doi.org/10.1158/1078-0432.CCR-14-3096.

40. Aumiller, V., Strobel, B., Romeike, M., Schuler, M., Stierstorfer, B.E., and Kreuz, S. (2017). Comparative analysis of lysyl oxidase (like) family members in pulmonary fibrosis. Sci. Rep. *7*, 149. https://doi.org/10.1038/s41598-017-00270-0.

41. Rudman-Melnick, V., Adam, M., Stowers, K., Potter, A., Ma, Q., Chokshi, S.M., Vanhoutte, D., Valiente-Alandi, I., Lindquist, D.M., Nieman, M.L., et al. (2024). Single-cell sequencing dissects the transcriptional identity of activated fibroblasts and identifies novel persistent distal tubular injury patterns in kidney fibrosis. Sci. Rep. *14*, 439. https://doi.org/10.1038/s41598-023-50195-0.

42. Sertie, A.L., Sossi, V., Camargo, A.A., Zatz, M., Brahe, C., and Passos-Bueno, M.R. (2000). Collagen XVIII, containing an endogenous inhibitor of angiogenesis and tumor growth, plays a critical role in the maintenance of retinal structure and in neural tube closure (Knobloch syndrome). Hum. Mol. Genet. *9*, 2051–2058. https://doi.org/10.1093/hmg/9.13.2051.

43. Sole-Boldo, L., Raddatz, G., Schutz, S., Mallm, J.P., Rippe, K., Lonsdorf, A.S., Rodriguez-Paredes, M., and Lyko, F. (2020). Single-cell transcriptomes of the human skin reveal age-related loss of fibroblast priming. Commun. Biol. *3*, 188. https://doi.org/10.1038/s42003-020-0922-4.

44. Xue, X., Wu, X., Fan, Y., Han, S., Zhang, H., Sun, Y., Yin, Y., Yin, M., Chen, B., Sun, Z., et al. (2024). Heterogeneous fibroblasts contribute to fibrotic scar formation after spinal cord injury in mice and monkeys. Nat. Commun. *15*, 6321. https://doi.org/10.1038/s41467-024-50564-x.

45. Moon, H.J., Finney, J., Xu, L., Moore, D., Welch, D.R., and Mure, M. (2013). MCF-7 cells expressing nuclear associated lysyl oxidase-like 2 (LOXL2) exhibit an epithelial-to-mesenchymal transition (EMT) phenotype and are highly invasive in vitro. J. Biol. Chem. *288*, 30000–30008. https://doi.org/10.1074/jbc.C113.502310.

46. Eyre, D.R., Paz, M.A., and Gallop, P.M. (1984). Cross-linking in collagen and elastin. Annu. Rev. Biochem. *53*, 717–748. https://doi.org/10.1146/annurev.bi.53.070184.003441.

47. Akam-Baxter, E.A., Bergemann, D., Ridley, S.J., To, S., Andrea, B., Moon, B., Ma, H., Zhou, Y., Aguirre, A., Caravan, P., et al. (2024). Dynamics of collagen oxidation and cross linking in regenerating and irreversibly infarcted myocardium. Nat. Commun. *15*, 4648. https://doi.org/10.1038/s41467-024-48604-7.

48. Akam-Baxter, E., Ridley, S.J., Moon, B.F., Caravan, P., and Sosnovik, D.E. (2025). Collagen Pyridinoline Cross-Links Are Absent in Reversible Myocardial Fibrosis. Circ. Res. *136*, 315–317. https://doi.org/10.1161/CIRCRESAHA.124.325406.

49. Lafouasse, L., Koutsogiannis, K., Dai, Y.E., Del Vecchio, L., Pedroni, A., Tsagkogiannis, D., Habicher, J., and Ampatzis, K. (2026). Time-dependent adaptations of damaged neurons and their microenvironment in the regenerating adult zebrafish spinal cord. Sci. Adv. *12*, eaea2882. https://doi.org/10.1126/sciadv.aea2882.

50. Baumann, H.J., Mahajan, G., Ham, T.R., Betonio, P., Kothapalli, C.R., Shriver, L.P., and Leipzig, N.D. (2020). Softening of the chronic hemi-section spinal cord injury scar parallels dysregulation of cellular and extracellular matrix content. J. Mech. Behav. Biomed. Mater. *110*, 103953. https://doi.org/10.1016/j.jmbbm.2020.103953.

51. Moeendarbary, E., Weber, I.P., Sheridan, G.K., Koser, D.E., Soleman, S., Haenzi, B., Bradbury, E.J., Fawcett, J., and Franze, K. (2017). The soft mechanical signature of glial scars in the central nervous system. Nat. Commun. *8*, 14787. https://doi.org/10.1038/ncomms14787.

52. Mollmert, S., Kharlamova, M.A., Hoche, T., Taubenberger, A.V., Abuhattum, S., Kuscha, V., Kurth, T., Brand, M., and Guck, J. (2020). Zebrafish Spinal Cord Repair Is Accompanied by Transient Tissue Stiffening. Biophys. J. *118*, 448–463. https://doi.org/10.1016/j.bpj.2019.10.044.

53. Rodriguez, H.M., Vaysberg, M., Mikels, A., McCauley, S., Velayo, A.C., Garcia, C., and Smith, V. (2010). Modulation of lysyl oxidase-like 2 enzymatic activity by an allosteric antibody inhibitor. J. Biol. Chem. *285*, 20964–20974. https://doi.org/10.1074/jbc.M109.094136.

54. Senk, A., and Djonov, V. (2021). Collagen fibers provide guidance cues for capillary regrowth during regenerative angiogenesis in zebrafish. Sci. Rep. *11*, 19520. https://doi.org/10.1038/s41598-021-98852-6.

55. Zhang, J., Liang, Y., Zeng, W., Gao, X., Wang, D., Mai, C., Lin, Z., Zhao, H., and Li, X. (2024). Inducing aortic aneurysm/dissection in zebrafish: evaluating the efficacy of beta-Aminopropionic Nitrile as a model. Anim. Cells Syst. *28*, 84–92. https://doi.org/10.1080/19768354.2024.2322055.

56. Alper, S.R., and Dorsky, R.I. (2022). Unique advantages of zebrafish larvae as a model for spinal cord regeneration. Front. Mol. Neurosci. *15*, 983336. https://doi.org/10.3389/fnmol.2022.983336.

57. Becker, C.J., Cigliola, V., Gillotay, P., Rich, A., De Simone, A., Han, Y., Di Talia, S., and Poss, K.D. (2023). In toto imaging of glial JNK signaling during larval zebrafish spinal cord regeneration. Development *150*, dev202076. https://doi.org/10.1242/dev.202076.

58. Li, Y., Han, W., Wu, Y., Zhou, K., Zheng, Z., Wang, H., Xie, L., Li, R., Xu, K., Liu, Y., et al. (2019). Stabilization of Hypoxia Inducible Factor-1alpha by Dimethyloxalylglycine Promotes Recovery from Acute Spinal Cord Injury by Inhibiting Neural Apoptosis and Enhancing Axon Regeneration. J. Neurotrauma *36*, 3394–3409. https://doi.org/10.1089/neu.2018.6364.

59. Gerri, C., Marin-Juez, R., Marass, M., Marks, A., Maischein, H.M., and Stainier, D.Y.R. (2017). Hif-1alpha regulates macrophage-endothelial interactions during blood vessel development in zebrafish. Nat. Commun. *8*, 15492. https://doi.org/10.1038/ncomms15492.

60. Jain, S.K., and Subrahmanyam, D. (1978). On the mechanism of phenylhydrazine-induced hemolytic anemia. Biochem. Biophys. Res. Commun. *82*, 1320–1324. https://doi.org/10.1016/0006-291x(78)90332-7.

61. Jopling, C., Sune, G., Faucherre, A., Fabregat, C., and Izpisua Belmonte, J.C. (2012). Hypoxia induces myocardial regeneration in zebrafish. Circulation *126*, 3017–3027. https://doi.org/10.1161/CIRCULATIONAHA.112.107888.

62. Saputra, F., Kishida, M., and Hu, S.Y. (2024). Oxidative stress induced by hydrogen peroxide disrupts zebrafish visual development by altering apoptosis, antioxidant and estrogen related genes. Sci. Rep. *14*, 14454. https://doi.org/10.1038/s41598-024-64933-5.

63. Koh, M.Y., Spivak-Kroizman, T., Venturini, S., Welsh, S., Williams, R.R., Kirkpatrick, D.L., and Powis, G. (2008). Molecular mechanisms for the activity of PX-478, an antitumor inhibitor of the hypoxia-inducible factor-1alpha. Mol. Cancer Ther. *7*, 90–100. https://doi.org/10.1158/1535-7163.MCT-07-0463.

64. Grant, C.E., Bailey, T.L., and Noble, W.S. (2011). FIMO: scanning for occurrences of a given motif. Bioinformatics *27*, 1017–1018. https://doi.org/10.1093/bioinformatics/btr064.

65. Chia, N.Y., Deng, N., Das, K., Huang, D., Hu, L., Zhu, Y., Lim, K.H., Lee, M.H., Wu, J., Sam, X.X., et al. (2015). Regulatory crosstalk between lineage-survival oncogenes KLF5, GATA4 and GATA6 cooperatively promotes gastric cancer development. Gut *64*, 707–719. https://doi.org/10.1136/gutjnl-2013-306596.

66. Hu, X., Li, T., Zhang, C., Liu, Y., Xu, M., Wang, W., Jia, Z., Ma, K., Zhang, Y., and Zhou, C. (2011). GATA4 regulates ANF expression synergistically with Sp1 in a cardiac hypertrophy model. J. Cell Mol. Med. *15*, 1865–1877. https://doi.org/10.1111/j.1582-4934.2010.01182.x.

67. Morin, S., Charron, F., Robitaille, L., and Nemer, M. (2000). GATA-dependent recruitment of MEF2 proteins to target promoters. EMBO J. *19*, 2046–2055. https://doi.org/10.1093/emboj/19.9.2046.

68. Mathison, M., Singh, V.P., Sanagasetti, D., Yang, L., Pinnamaneni, J.P., Yang, J., and Rosengart, T.K. (2017). Cardiac reprogramming factor Gata4 reduces postinfarct cardiac fibrosis through direct repression of the profibrotic mediator snail. J. Thorac. Cardiovasc. Surg. *154*, 1601–1610.e3. https://doi.org/10.1016/j.jtcvs.2017.06.035.

69. Tsissios, G., Leleu, M., Hu, K., Demirtas, A.E., Hu, H., Vinzens, S., Kawanishi, T., Skoufa, E., Valanju, A., Valente, A., et al. (2026). Species-specific oxygen sensing governs the initiation of vertebrate limb regeneration. Science *392*, eadw8526. https://doi.org/10.1126/science.adw8526.

70. Gilad, G.M., and Gilad, V.H. (2001). Beta-aminopropionitrile treatment can accelerate recovery of mice after spinal cord injury. Eur. J. Pharmacol. *430*, 69–72. https://doi.org/10.1016/s0014-2999(01)01354-1.

71. Sun, S., Liu, Z., Li, X., Jia, J., Zhang, G., Yang, C., Jiang, Q., and Zou, Y. (2020). Characterization of a nap1l1 transgenic reporter in zebrafish. Gene *735*, 144388. https://doi.org/10.1016/j.gene.2020.144388.

72. Bernardos, R.L., and Raymond, P.A. (2006). GFAP transgenic zebrafish. Gene Expr. Patterns *6*, 1007–1013. https://doi.org/10.1016/j.modgep.2006.04.006.

73. Zhao, L., Borikova, A.L., Ben-Yair, R., Guner-Ataman, B., MacRae, C.A., Lee, R.T., Burns, C.G., and Burns, C.E. (2014). Notch signaling regulates cardiomyocyte proliferation during zebrafish heart regeneration. Proc. Natl. Acad. Sci. USA *111*, 1403–1408. https://doi.org/10.1073/pnas.1311705111.

74. Shin, J., Park, H.C., Topczewska, J.M., Mawdsley, D.J., and Appel, B. (2003). Neural cell fate analysis in zebrafish using olig2 BAC transgenics. Methods Cell Sci. *25*, 7–14. https://doi.org/10.1023/B:MICS.0000006847.09037.3a.

75. Ando, K., Fukuhara, S., Izumi, N., Nakajima, H., Fukui, H., Kelsh, R.N., and Mochizuki, N. (2016). Clarification of mural cell coverage of vascular endothelial cells by live imaging of zebrafish. Development *143*, 1328–1339. https://doi.org/10.1242/dev.132654.

76. Schneider, C.A., Rasband, W.S., and Eliceiri, K.W. (2012). NIH Image to ImageJ: 25 years of image analysis. Nat. Methods *9*, 671–675. https://doi.org/10.1038/nmeth.2089.

77. Hao, Y., Stuart, T., Kowalski, M.H., Choudhary, S., Hoffman, P., Hartman, A., Srivastava, A., Molla, G., Madad, S., Fernandez-Granda, C., and Satija, R. (2024). Dictionary learning for integrative, multimodal and scalable single-cell analysis. Nat. Biotechnol. *42*, 293–304. https://doi.org/10.1038/s41587-023-01767-y.

78. Elizarraras, J.M., Liao, Y., Shi, Z., Zhu, Q., Pico, A.R., and Zhang, B. (2024). WebGestalt 2024: faster gene set analysis and new support for metabolomics and multi-omics. Nucleic Acids Res. *52*, W415–W421. https://doi.org/10.1093/nar/gkae456.

79. Bailey, T.L., Johnson, J., Grant, C.E., and Noble, W.S. (2015). The MEME Suite. Nucleic Acids Res. *43*, W39–W49. https://doi.org/10.1093/nar/gkv416.

80. Fang, P., Lin, J.F., Pan, H.C., Shen, Y.Q., and Schachner, M. (2012). A surgery protocol for adult zebrafish spinal cord injury. J. Genet. Genomics *39*, 481–487. https://doi.org/10.1016/j.jgg.2012.07.010.

81. Becker, T., and Becker, C.G. (2001). Regenerating descending axons preferentially reroute to the gray matter in the presence of a general macrophage/microglial reaction caudal to a spinal transection in adult zebrafish. J. Comp. Neurol. *433*, 131–147. https://doi.org/10.1002/cne.1131.

82. Becker, C.G., Lieberoth, B.C., Morellini, F., Feldner, J., Becker, T., and Schachner, M. (2004). L1.1 is involved in spinal cord regeneration in adult zebrafish. J. Neurosci. *24*, 7837–7842. https://doi.org/10.1523/JNEUROSCI.2420-04.2004.

83. Jia, W., Wu, W., Yang, D., Xiao, C., Huang, M., Long, F., Su, Z., Qin, M., Liu, X., and Zhu, Y.Z. (2018). GATA4 regulates angiogenesis and persistence of inflammation in rheumatoid arthritis. Cell Death Dis. *9*, 503. https://doi.org/10.1038/s41419-018-0570-5.

84. Yi, X., Zhou, Y., Chen, Y., Feng, X., Liu, C., Jiang, D.S., Geng, J., Li, X., Jiang, X., and Fang, Z.M. (2021). The Expression Patterns and Roles of Lysyl Oxidases in Aortic Dissection. Front. Cardiovasc. Med. *8*, 692856. https://doi.org/10.3389/fcvm.2021.692856.

85. Guo, S., Zhang, Y., Zhou, T., Wang, D., Weng, Y., Chen, Q., Ma, J., Li, Y.P., and Wang, L. (2018). GATA4 as a novel regulator involved in the development of the neural crest and craniofacial skeleton via Barx1. Cell Death Differ. *25*, 1996–2009. https://doi.org/10.1038/s41418-018-0083-x.

86. Maheras, A.L., Dix, B., Carmo, O.M.S., Young, A.E., Gill, V.N., Sun, J.L., Booker, A.R., Thomason, H.A., Ibrahim, A.E., Stanislaw, L., et al. (2018). Genetic Pathways of Neuroregeneration in a Novel Mild Traumatic Brain Injury Model in Adult Zebrafish. eNeuro *5*. https://doi.org/10.1523/ENEURO.0208-17.2017.

87. Mjaavatten, A. (2025). Curvature of a 1D curve in a 2D or 3D space. (https://www.mathworks.com/matlabcentral/fileexchange/69452-curvature-of-a-1d-curve-in-a-2d-or-3d-space) MATLAB Central File Exchange.

STAR★METHODS

KEY RESOURCES TABLE

REAGENT or RESOURCE	SOURCE	IDENTIFIER
Antibodies		
Rabbit anti-GFAP	Sigma-Aldrich	Cat#G9269; RRID:AB_477035
Rabbit anti-GFP	Molecular Probes	Cat#A11122; RRID:AB_221569
Rabbit anti-SOX2	Abcam	Cat#ab97959; RRID:AB_2341193
Mouse anti-PCNA	Sigma-Aldrich	Cat#P8825; RRID:AB_477413
Mouse anti-HuC/D	Molecular Probes	Cat#A-21271; RRID:AB_221448
Mouse anti-GFAP	Zebrafish International Resource Center	Cat#Zrf1; RRID:AB_10013806
Rabbit Anti-Fibronectin	Sigma-Aldrich	Cat#F3648; RRID:AB_476976
Mouse anti-Vimentin	Proteintech	Cat#60330; RRID:AB_2880695
Rabbit anti-Collagen I	Abcam	Cat#ab34710; RRID:AB_731684
Mouse Anti-Acetylated α-Tubulin	Sigma-Aldrich	Cat#T6793; RRID:AB_477585
Mouse Anti-Znp-1	DSHB	Cat#znp-1; RRID:AB_2315626
Mouse Anti-SV2	DSHB	Cat#SV2; RRID:AB_2315387
Mouse Anti-LOXL2	Proteintech	Cat#67139-1-Ig; RRID:AB_3085455
Rabbit Anti-HIF1α	Proteintech	Cat#20960-1-AP; RRID:AB_10732601
Alexa Fluor 488 Goat anti-Rabbit IgG (H + L)	Thermo Fisher Scientific	Cat#A-11034; RRID:AB_2576217
Alexa Fluor 488 Goat anti-Mouse IgG (H + L)	Thermo Fisher Scientific	Cat#A-11001; RRID:AB_2534069
Alexa Fluor 546 Goat anti-Rabbit IgG (H + L)	Thermo Fisher Scientific	Cat#A-11035; RRID:AB_143051
Alexa Fluor 546 Goat anti-Mouse IgG (H + L)	Thermo Fisher Scientific	Cat#A-11030; RRID:AB_144695
Alexa Fluor 594 Goat anti-Rabbit IgG (H + L)	Thermo Fisher Scientific	Cat#A-11037; RRID:AB_2534095
Alexa Fluor 594 Goat anti-Mouse IgG (H + L)	Thermo Fisher Scientific	Cat#A-11032; RRID:AB_141672
Sheep anti-DIG	Sigma-Aldrich	Cat#11093274910; RRID:AB_2313640
Chemicals, peptides, and recombinant proteins		
5-ethynyl-2′-deoxyuridine	Sigma-Aldrich	Cat#900584
Dimethyloxalylglycine (DMOG)	Sigma-Aldrich	Cat#D3695
Hydrogen peroxide	Thermo Fisher Scientific	Cat#H325-500
Phenylhydrazine	Sigma-Aldrich	Cat#114715
PX-478	TargetMol	Cat#T6961
β-Aminopropionitrile (BAPN)	Selleckchem	Cat#E4275
TMR-NB probe	Akam-Baxter et al.[47]	N/A
TMR-O probe	Akam-Baxter et al.[47]	N/A
Alexa Fluor 594 azide	Thermo Fisher Scientific	Cat#A10270
MS-222	Sigma-Aldrich	Cat#A5040
Paraformaldehyde	Sigma-Aldrich	Cat#P6148
Bouin's Fixative Solution	Ricca Chemical	Cat#1120–16
Tris base	RPI	Cat#T60040
Copper sulfate	Sigma-Aldrich	Cat#C1297
Potassium chloride	Sigma-Aldrich	Cat# P3911
Magnesium chloride	Sigma-Aldrich	Cat#M8266
Sodium chloride	RPI	Cat#S23020
Sucrose	Sigma-Aldrich	Cat#S9378
Triton X-100	Sigma-Aldrich	Cat#X100
RNase inhibitor	New England Biolabs	Cat#M0307S

(*Continued on next page*)

Continued

REAGENT or RESOURCE	SOURCE	IDENTIFIER
Calcium chloride	Sigma-Aldrich	Cat#C70
HEPES	Thermo Fisher Scientific	Cat#BP310
Glucose	Sigma-Aldrich	Cat#GRM6549
Phosphomolybdic acid	Tokyo Chemical Industry (TCI)	Cat#P1910
Aniline blue	HIMEDIA	Cat#GRM901
Orange G	Thermo Fisher Scientific	Cat#S25453
Acid fuchsin	Thermo Fisher Scientific	Cat#227900250
Wisteria floribunda agglutinin (WFA)	Thermo Fisher Scientific	Cat#L32481
Picrosirius Red Solution	Abcam	Cat#ab246832
Alexa Fluor 594 Biocytin	Thermo Fisher Scientific	Cat#A12922
DAPI	Thermo Fisher Scientific	Cat#D3571
Matrigel	Thermo Fisher Scientific	Cat#354230
Y-27632	STEMCELL Technologies	Cat#72308
Versene	Gibco	Cat#15040066
Essential 6™ Medium	Gibco	Cat#A1516401
StemFlex™ medium	Gibco	Cat#A3349401
B27 supplement	Gibco	Cat#12587010
N-2 supplement	Thermo Fisher Scientific	Cat#17502048
Y-27632	Tocris	Cat#1254
Laminin	Sigma-Aldrich	Cat#L2020
Retinoic acid	Thermo Fisher Scientific	Cat#044540.77
Human FGF-basic (FGF-2/bFGF) (146 aa) Recombinant Protein, PeproTech®	PeproTech	Cat#100-18C
TrypLE™	Gibco	Cat#12604013
Human BMP-4 Recombinant Protein, PeproTech®	PeproTech	Cat#120-05ET
Human CNTF Recombinant Protein, PeproTech®	PeproTech	Cat#450–13
Human EGF Recombinant Protein	Thermo Fisher Scientific	Cat#PHG0311
SuperScript III First-Strand Synthesis System	Sigma-Aldrich	Cat#T7924
Poly-L-Lysine	Ted Pella	Cat#18026
Fluoromount-G	Thermo Fisher Scientific	Cat#00–4958-02
Dimethyl sulfoxide (DMSO)	Sigma-Aldrich	Cat#472301
Trypsin-EDTA, 0.25%	Thermo Fisher Scientific	Cat#25200072
T7 RNA polymerase	New England BioLab	Cat#M0251
BCIP (5-bromo-4-chloro-3-indolyl-phosphate)	Roche	Cat#11697471001
NBT (nitroblue tetrazolium)	Roche	Cat#11383213001
Gelfoam gelatine sponge	Pfizer	Cat#09–0315-08
Critical commercial assays		
Evercode™ Nuclei Fixation v2	Parse Biosciences	Cat#ECF2103
Evercode™ WT Mini v2	Parse Biosciences	Cat#ECW02010
Deposited data		
snRNA-seq dataset #1 resource	This study	GEO: GSE316679
Experimental models: Organisms/strains		
Ekkwill zebrafish	Ekkwill Breeders (FL)	EKW
Tg(-14.8gata4:EGFP)	Heicklen-Klein et al.[30]	ZDB-TGCONSTRCT-070117–5
Tg(HuC:mCherry)	Sun et al.[71]	ZDB-TGCONSTRCT-210714–3
Tg(gfap:H2A-mCherry)	Becker et al.[57]	ZDB-TGCONSTRCT-250404–2
Tg(gfap:EGFP)	Bernardos and Raymond[72]	ZDB-TGCONSTRCT-070117–154
Tg(-14.8gata4:dsRedII)	Zhao et al.[73]	ZDB-TGCONSTRCT-140611–1

(*Continued on next page*)

Continued

REAGENT or RESOURCE	SOURCE	IDENTIFIER
Tg(olig2:EGFP)	Shin et al.[74]	ZDB-TGCONSTRCT-070117–167
TgBAC(pdgfrb:mCherry)	Ando et al.[75]	ZDB-TGCONSTRCT-160609–1
gata4$^{wcm6/wcm6}$	Sam et al.[33]	ZDB-ALT-210322–5
Tg(hsp70L:gata4-P2A-EGFP)	This study	N/A
Oligonucleotides		
Primers for quantitative PCR (qPCR)	Integrated DNA Technologies	See Table S11
Software and algorithms		
Fiji (ImageJ v2.16.0/1.54)	Schneider et al.[76]	https://imagej.net/software/fiji/
GraphPad Prism (v10.3.1)	GraphPad Software Inc.	https://www.graphpad.com/
Seurat v5 (R v4.2.1)	Hao et al.[77]	https://satijalab.org/seurat/
WebGestalt (2024)	Elizarraras et al.[78]	https://webgestalt.org
MEME Suite/FIMO	Grant et al.[79]	https://meme-suite.org
NIS-Elements General Analysis 3 (GA3)	Nikon Instruments Inc.	https://www.nisoftware.net/
SnapGene	Dotmatics	www.snapgene.com
Bruker NanoScope Analysis	Bruker	RRID: SCR_026153
Custom Python code for *in situ* hybridization quantification	This paper	https://doi.org/10.5281/zenodo.21926882
Custom Python code for motif analysis	This paper	https://doi.org/10.5281/zenodo.21926901; https://doi.org/10.5281/zenodo.21926910
Single-nucleus RNA-sequencing data	This paper	GEO: GSE316679

EXPERIMENTAL MODEL AND STUDY PARTICIPANT DETAILS

Zebrafish

Wild-type, mutant, or transgenic zebrafish of the Ekkwill (EK) strain were used for all experiments. Control and experimental animals were female and male clutch mates aged 3 to 9 months, measuring ~2.5 cm in length. Zebrafish were raised under standard laboratory conditions at 28.5 °C. Experimental fish and size-matched control siblings with balanced sex representation were used for all assays. All experiments were conducted in accordance with guidelines established by the Institutional Animal Care and Use Committee and the Institutional Biosafety Committee at Vanderbilt University (protocol M2400047), as well as French regulations for animal care, with approval from the local Animal Care and Use Committee of the Institute of Biology Valrose (Nice) and the French Ministry of Research (no. 43195–2023060312002720). The following previously published lines were used for this study: *Tg(-14.8gata4:EGFP)*[30], *Tg(HuC:mCherry)*,[71] *Tg(gfap:H2A-mCherry)*,[57] *Tg(gfap:EGFP)*,[72] *Tg(-14.8gata4:dsRedII)*,[73] *Tg(olig2:EGFP)*,[74] *TgBAC(pdgfrb:mCherry)*,[33] *gata4*$^{wcm6/wcm6}$.[33]

Generation of *hsp70l:gata4-P2A-EGFP* zebrafish

The zebrafish *gata4* coding sequence was amplified by PCR using the primers *gata4*-F (5′-ATGTATCAAGGTGTAACGAT-3′) and *gata4*-R (5′-GGCTGTTCCACACTTCACTC-3′). The amplified fragment was assembled with appropriate homology arms and cloned into an *hsp70l:P2A-EGFP* expression vector using Gateway LR Clonase II Enzyme Mix (Thermo Fisher Scientific, Cat#11791020). The resulting plasmid was co-injected with I-SceI meganuclease into one-cell-stage wild-type embryos. Multiple founders were identified, propagated, and screened for germline transmission based on EGFP expression following heat-shock induction. A single transgenic line was selected for subsequent experiments. The full name of this line is *Tg(hsp70l:gata4-P2A-EGFP)*^{vu723}.

METHOD DETAILS

Spinal cord injury

Adult zebrafish were anesthetized in 0.02% aminobenzoic-acid-ethyl methyl-ester (MS-222, Sigma Aldrich, Cat#A5040) buffered to pH 7.0. Scales were removed, and a small incision was made through the dorsal musculature using fine scissors to expose the vertebral column, which was then transected midway between the dorsal fin and the operculum.[11,80] Full spinal cord transection was visually confirmed at the time of surgery, and complete loss of swimming ability at 1, 2 and 3 dpi.

Zebrafish larvae at 3 dpf were anesthetized in 0.02% MS-222. Larvae were transferred to a Petri dish and following removal of excess water, they were placed in a lateral position. The tip of a sharp 30½ G syringe needle was used to inflict a transection injury on the dorsal part of the trunk at the level of the 15th myotome.[19]

Immunofluorescence

At the time of analysis, spinal cords were collected, fixed overnight in 4% paraformaldehyde (Sigma-Aldrich, Cat#P6148), rinsed in phosphate buffer, and cryoprotected in 20% sucrose (Sigma-Aldrich, Cat#S9378). Samples were embedded in OCT (Tissue-Tek), frozen on dry ice, and cryosectioned at 20 μm (longitudinal) or 16 μm (transverse). For standard immunofluorescence, sections were rehydrated in phosphate buffer, permeabilized in Triton X-100 (Sigma-Aldrich, Cat#X100), and blocked for 1 h at room temperature in bovine serum albumin-blocking reagent. Sections were incubated overnight with primary antibodies diluted in blocking reagent, washed in phosphate buffer, and incubated for 1 h with secondary antibodies and DAPI (Thermo Fisher Scientific, Cat#D3571, 1:5000). Following washes, sections were mounted using Fluoromount-G (Invitrogen, Cat#00-4958-02). LOXL2 staining followed the same procedures with the addition of an antigen retrieval step. Sections underwent antigen retrieval in sodium citrate buffer at 98 °C for 6 min and were allowed to cool for 20 min before proceeding with standard immunofluorescence. Primary antibodies included: rabbit anti-GFP (Life Technologies, Cat#A11122, 1:200), mouse anti-GFAP (ZIRC, Cat#Zrf1, 1:1000), rabbit anti-GFAP (Sigma-Aldrich, Cat#G9269, 1:200), rabbit anti-SOX2 (Abcam, Cat#ab97959, 1:200), mouse anti-HuC/D (Invitrogen, Cat#A-21271, 1:100), mouse anti-Acetylated-α-tubulin (Sigma-Aldrich, Cat#T6793, 1:1000), mouse anti-PCNA (Sigma-Aldrich, Cat#P8825, 1:200), rabbit anti-Fibronectin (Sigma-Aldrich, Cat#F3648, 1:200), mouse anti-Vimentin (Proteintech, Cat#60330-1-Ig, 1:500), rabbit anti-Collagen I (Abcam, Cat#ab34710, 1:200), mouse anti-LOXL2 (Proteintech, Cat#67139-1-Ig), mouse anti-Znp-1 (DSHB, Cat#AB2315626, 1:150), mouse anti-SV2 (DSHB, Cat#AB2315387, 1:150), rabbit anti-HIF-1α (Proteintech, Cat#20960-1-AP, 1:500). Secondary antibodies (Life Technologies, 1:200) were Alexa Fluor 488/546/594 goat anti-rabbit or goat anti-mouse. All confocal images were acquired on Zeiss LSM 880 and Nikon AX/R with NSPARC detection microscopes.

In situ hybridization

In situ hybridization was performed on 20 μm longitudinal cryosections. Briefly, spinal cords were fixed in 4% paraformaldehyde, cryoprotected in sucrose, embedded in OCT, and cryosectioned at 20 μm. Sections were treated with proteinase K and hybridized overnight at 65 °C with DIG-labeled antisense RNA probes. To generate probes, gBlock fragments containing target sequences upstream of a T7 upstream regulatory region were ordered from Integrated DNA Technologies (IDT). Probes were transcribed using T7 RNA polymerase (New England BioLab, Cat#M0251). *In situ* hybridization signals were visualized by immunoassay using an anti-DIG-AP (alkaline phosphatase) antibody (Sigma-Aldrich, Cat#11093274910) and subsequent catalytic color reaction with NBT (nitroblue tetrazolium, Sigma-Aldrich, Cat#11383213001)/BCIP (5-bromo-4-chloro-3-indolyl-phosphate, Sigma-Aldrich, Cat#11383221001). Sections were imaged using an Olympus BX41TF microscope.

AFOG, picrosirius and WFA staining

Fish underwent spinal cord transection and were allowed to recover for 2 weeks. At 2 wpi, animals were euthanized, and spinal cords were dissected, fixed overnight in 4% paraformaldehyde, cryoprotected in 20% sucrose (Sigma-Aldrich, Cat# S9378) following rinsing in phosphate buffer, embedded, and sectioned longitudinally at 20 μm.

For AFOG staining, sections were hydrated in deionized water for 10 min and incubated in preheated Bouin's Fixative Solution (Ricca Chemical, Cat#1120–16) for 2 h at 60 °C. Slides were then allowed to incubate for an additional hour at room temperature, followed by gentle washing under constant running water for 30 min. Sections were incubated in 1% phosphomolybdic acid (Tokyo Chemical Industry, Cat#P1910) for 5 min and rinsed in deionized water for 5 min. Slides were stained for 5 min in AFOG solution containing 0.25 g aniline blue (HIMEDIA, Cat#GRM901), 0.5 g orange G (Thermo Fisher Scientific, Cat#S25453), and 0.75 g acid fuchsin (Thermo Fisher Scientific, Cat#227900250) dissolved in 50 mL total volume. Sections were then rinsed twice in DI water for 5 min each, dehydrated through graded ethanol washes (75%, 95%, and 100% ethanol; two washes each for 5 min), cleared in xylene for 2 min, briefly air-dried, and mounted with mineral oil.

For Picrosirius Red staining, 20 μm cryosections were rehydrated in deionized water. Slides were then incubated in Picrosirius Red solution (Abcam, Cat#ab246832) for 1 h at room temperature. Following staining, sections were briefly washed twice in 0.5% acetic acid, dehydrated through graded ethanol solutions (75%, 90%, 100%), and cleared in xylene twice for 2 min each. Slides were then mounted using mineral oil.

For Wisteria floribunda agglutinin (WFA) staining, tissue sections were permeabilized, washed three times in PBS, and blocked using the same conditions described for immunohistochemistry. Samples were then incubated overnight at 4 °C with WFA conjugate (Invitrogen, Cat#L32481; 1:500) diluted in blocking solution. The following day, sections were washed three times for 5 min each in PBS and mounted with mineral oil before proceeding with imaging.

EdU labeling

Adult zebrafish received an intraperitoneal injection of 5-ethynyl-2′-deoxyuridine (EdU, Millipore Sigma-Aldrich, Cat#900584; 10 μL, 10 μM) at 2 weeks post-injury. Animals were euthanized 12 h later, and spinal cord tissue was collected and fixed overnight in 4% paraformaldehyde at 4 °C. Following acetone permeabilization, EdU detection was performed using a click chemistry reaction containing Tris buffer pH 8.5 (RPI, Cat#T60040), $CuSO_4$ (Sigma-Aldrich, Cat#C1297), Alexa Fluor 594 azide (Thermo Fisher Scientific, Cat#A10270), and freshly prepared ascorbic acid in PBS. Samples were incubated for 48 h at 4 °C with gentle agitation and protected from light. Following labeling, confocal images were acquired on a Nikon AX/R with NSPARC detection microscope.

Biocytin axon tracing

Adult zebrafish were anesthetized, and biocytin axon tracing was performed as previously described.[12,81,82] Briefly, a second spinal cord transection was performed approximately 4 mm rostral to the original lesion site. A Gelfoam sponge (Pfizer, Cat#09–0315-08) soaked in Alexa Fluor 594 Biocytin (Thermo Fisher Scientific, Cat#A12922) was placed at the lesion site. The incision was then closed and sealed using Vetbond tissue adhesive (3M, Cat#1469SB).

Drug and probe treatments

For β-aminopropionitrile (BAPN; Selleckchem, Cat#E4275) treatment, adult fish were allowed to recover for 1 day following spinal cord injury and then transferred to 300 mL of system water supplemented with an air stone. Experimental animals were treated with BAPN at a final concentration of 1.0 mM, and BAPN-containing water was refreshed every other day. Control and treated animals underwent water changes on the same schedule. Treatment was maintained under continuous exposure from 2 to 14 dpi, after which fish were euthanized, and spinal cord tissue was collected for histological analysis.

For TMR-O and TMR-NB treatments, at 2 wpi fish were injected intraperitoneally with 10 μL of 0.1 mM TMR-O or TMR-NB. Animals were kept in the dark for 4 h following injection, then euthanized, and tissues were processed for histological analysis.

For larval drug exposure experiments, dimethyloxalylglycine (DMOG; Sigma-Aldrich, Cat#D3695) was dissolved in DMSO to a stock concentration of 2.0 mg/mL and working solutions (100 or 200 μM) were prepared by dilution of the stock in egg water. Phenylhydrazine (PHZ; Sigma-Aldrich, Cat# 114715) was dissolved in DMSO to a stock concentration of 2.0 mg/mL and working concentrations (13.8 or 27.6 μM) were prepared by dilution in egg water. Hydrogen peroxide (H_2O_2; Thermo Fisher Scientific, Cat#H325-500) was added directly to egg water to prepare working solutions at a final concentration of 1.0, 2.0 or 3.0 mM. PX-478 (TargetMol, Cat#T6961) was dissolved in DMSO and was added directly to egg water at a final concentration of 10 μM. Larvae were treated in 24-well plates, with five larvae per well in a total volume of 1.0. mL and were subjected to either continuous drug exposure or overnight treatment.

iPSC maintenance

The KOLF2.1J iPSC line was used for all experiments. Undifferentiated iPSCs were maintained in StemFlex medium (Gibco, Cat#A3349401) on growth factor-reduced Matrigel (Corning)-coated 6-well plates. Cells were passaged using Versene (Gibco, Cat#15040066) upon reaching 60–80% confluency.

iPSC differentiation into astrocytes

To minimize variability in astrocyte generation, manually isolated neural progenitor cells were used as the starting population. iPSCs were dissociated with Versene and seeded into low-attachment 6-well plates at a density of 4×10^5 cells per well to generate embryoid bodies (EBs) in Essential 6 (E6) medium (Gibco, Cat#A1516401) supplemented with N2 (Gibco, Cat#E6N2) and 10 μM Y-27632 (Tocris, Cat#1254).

Neural differentiation was induced by dual SMAD inhibition for 7 days. EBs were then plated onto growth factor-reduced Matrigel-coated plates in E6N2 supplemented with 1 μg/mL laminin (Sigma-Aldrich, Cat#L2020). After an additional 7 days, neural progenitor cells were manually isolated from neural rosettes and expanded as neurospheres in suspension culture for 7 days in E6N2 supplemented with B27 minus retinoic acid (Gibco, Cat#12587010) and 20 ng/mL FGF2 (PeproTech, Cat#100-18C).

Neurospheres were subsequently dissociated into single cells using TrypLE (Gibco, Cat#12604013) and plated onto growth factor-reduced Matrigel-coated 6-well plates in E6N2 supplemented with B27 minus retinoic acid, 10 ng/mL BMP4 (PeproTech, Cat#120-05ET), and 20 ng/mL FGF2 (astrocyte medium) to promote astroglial differentiation. Medium was changed every 48 h, and cells were passaged upon reaching approximately 80% confluency.

For DMOG treatment experiments, human astrocytes were replated at a ratio of one well of a 6-well plate to six wells of a 12-well plate and maintained in E6 medium supplemented with 10 ng/mL CNTF (PeproTech, Cat#PHG0311) and 10 ng/mL EGF (PeproTech, Cat#450–13) until treatment. Differentiated human astrocytes were treated with 1.0 mM DMOG for 24 h. Following treatment, cells were fixed in 4% paraformaldehyde (PFA) and processed for immunofluorescence staining. HIF1-α expression was detected using a primary antibody against HIF1-α (Proteintech, Cat#20960-1-AP, 1:500), and nuclei were counterstained with DAPI. Images were acquired using a Leica DMi8 epifluorescence microscope and analyzed using Fiji/ImageJ.

Zebrafish spinal cord cell culture

Adult zebrafish were anesthetized, sacrificed and spinal cords were removed and placed in sterile phosphate buffer until all dissections were completed. Spinal cords were added to 2.0 mL of room temperature phosphate buffer for 2 min in a tube coated with 4% bovine serum albumin after which samples were moved to a 37 °C water bath for 2 min. Then, 600 μL of trypsin was added to the samples and cells were dissociated for no more than 10 min by constant pipetting. After dissociation, 2.0 mL of prewarmed astrocyte medium was added to the samples to terminate trypsin action. Dissociated cells were spun down at 4 °C and 600×*g* for 5 min, supernatant was removed and cells were resuspended in fresh culture medium consisting of 90% astrocyte medium, 10% fetal bovine serum, and 1:1000 Y-27632 (ROCK inhibitor, STEMCELL Technologies, Cat#72308). After resuspension cells were plated on 6-well plates coated in poly-L-lysine (Sigma-Aldrich, Cat#P4707) and Matrigel (Thermo Fisher Scientific, Cat#354230). Cells were treated with 1.0 mM DMOG for 24 h, then qRT-PCR was performed.

Quantitative real time PCR

Total RNA was extracted using TRIzol reagent (Sigma, Cat#T7924) and reverse-transcribed into cDNA using the SuperScript III First-Strand Synthesis System (Invitrogen, Cat#18080051). Quantitative real time PCR (qRT-PCR) was performed on a Bio-Rad CFX96 Real-Time PCR System. Gene expression levels were normalized to housekeeping genes (*GAPDH* for human genes and *β-actin* for zebrafish genes), and relative expression was calculated using the $2^{-\Delta\Delta Ct}$ method. Primer sequences were as follows: Human *GATA4*-F: 5′-CAGTCTACGTGCCCACACC-3′[83]; Human *GATA4*-R: 5′-TCCCGCCTGGCTCCAT-3′[83]; Human *LOXL2*-F: 5′-CTGCAAGTTCAATGCCGAGT-3′[84]; Human *LOXL2*-R: 5′-TCTCCACCAGCACCTCCACTC-3′[84]; Human *GAPDH*-F: 5′-CCAGAACAT CATCCCTGCCT-3′; Human *GAPDH*-R: 5′- CCTGCTTCACCACCTTCTTG-3′; Zebrafish *gata4*-F: 5′-CGGGTGGGTTTATCCT-3′[85]; Zebrafish *gata4*-R: 5′-ATCGCCGACTGACCTT-3′[85]; Zebrafish *loxl2b*-F: 5′-AAGCAGGGATTTACACTTCGGA-3′[86]; Zebrafish *loxl2b*-R: 5′-AGCCAGCATAATGA
CAGAGGC-3′[86]; Zebrafish *β-actin*-F: 5′-GACAACGGCTCCGGTATG-3′; Zebrafish *β-actin*-R: 5′-CATGCCAACCATCACTCC-3′.

Swim assays

To assess swim capacity, groups of fish were placed in a 5.0 L swim tunnel respirometer (Loligo, Cat#SW100605L, 120 V/60 Hz), as previously described.[18] Following a 20-min acclimation period at a low, constant water current, the flow velocity was increased every two minutes. Fish were allowed to swim against the current until exhaustion. Exhausted animals were removed from the chamber without disturbing the remaining fish, while others continued to swim. For each fish that reached exhaustion, swim time in minutes and the corresponding water velocity in cm/s were recorded and used as measurement of swim capacity. After all fish swam to exhaustion, they were allowed to recover and then placed back in recirculating water.

Atomic force microscopy

At 2 wpi, spinal cords were dissected and incubated for 1 h on ice in an artificial cerebrospinal fluid (aCSF)–like buffer containing 34 mM NaCl (RPI, Cat#S23020), 2.9 mM KCl (Sigma-Aldrich, Cat# P3911), 1.2 mM $MgCl_2$ (Sigma-Aldrich, Cat#M8266), 2.1 mM $CaCl_2$ (Sigma-Aldrich, Cat#C70), 10 mM HEPES (Thermo Fisher Scientific, Cat#BP310), 10 mM glucose (Sigma-Aldrich, Cat#GRM6549); pH 7.8 – supplemented with protease inhibitors – with gentle inversion. Samples were then cryoprotected in 20% sucrose, embedded in OCT, and sectioned at 30 μm. Sections were collected on poly-L-lysine–coated slides (Ted Pella, Cat#18026) and stored at −80 °C until atomic force microscopy (AFM) measurements. Prior to AFM analysis, sections were briefly thawed, washed in phosphate buffer, and kept hydrated in a humidity chamber using a hydrophobic barrier pen. AFM measurements were performed using a Bruker Dimension Icon microscope equipped with Bruker SPM-SPH 5 μm spherical probes. Thermal noise calibration was performed before each measurement. For each sample, 3–12 nanoindentations were acquired at three distinct locations within the lesion core.

Raw deflection–height data were converted to force–indentation curves and fit in *Bruker NanoScope Analysis* software to the Hertz–Spherical contact model:

$$F = A\,\delta^{3/2}, A = \frac{4}{3}E_{\text{eff}}R^{1/2}$$

where F is the applied force, δ is the indentation depth, E_eff is the effective Young's modulus, and R is the probe radius. The apparent tissue Young's modulus (E_s) was then derived from the fitting constant A according to:

$$E_s = \frac{3A}{4R^{1/2}}\left(1 - \nu_s^2\right)$$

where ν_s is the Poisson's ratio of the sample (0.4). Stiffness values (E_s) were reported in Pascals (Pa).

Body curvature analysis

Adult wild type and *gata4*$^{wcm6/wcm6}$ zebrafish were briefly anesthetized in 0.02% MS-222 (Sigma-Aldrich) and lateral images were obtained before spinal cord injury and subsequently at 2, 4 and 6 wpi. Curvature was calculated in MATLAB using the Curvature function of the *Curvature of a 1D curve in a 2D or 3D space* script.[87] Curvature analysis was performed blinded by tracing the XY coordinates along the dorsal body outline between the operculum and the caudal fin for each individual fish.

Single-nucleus RNA sequencing

Spinal cord segments (2.0 mm anterior and posterior to the injury site) were dissected from *gata4*$^{wcm6/wcm6}$ and wild-type zebrafish at 2 wpi, flash-frozen, and stored at −80 °C. Nuclei isolation was adapted from a previously established protocol.[53] All solutions, reagents, and tools were pre-chilled and maintained on ice throughout the procedure. Nuclei Isolation Buffer 1 (NIM1) consisted of 250 mM sucrose (Sigma-Aldrich, Cat#S0389), 25 mM KCl (Sigma-Aldrich, Cat#P3911), 5 mM $MgCl_2$ (Sigma-Aldrich, Cat#M8266), and 10 mM Tris (pH 8.0; RPI, Cat#T60040) prepared in RNase-free water. Nuclei Isolation Buffer 2 (NIM2) was prepared by supplementing NIM1 with 1 μM DTT, 0.4 U/μL RNase inhibitor (New England Biolabs, Cat#M0307S), and 0.1% Triton X-100 (Sigma Aldrich, Cat#X100). A swinging-bucket centrifuge was pre-cooled to 4 °C prior to sample processing. Tissue samples were incubated in cold

NIM2 buffer and gently dissociated by trituration on ice, followed by centrifugation at 200×*g* for 10 min at 4 °C. The resulting pellet was resuspended in Nuclei Buffer containing 0.75% bovine serum albumin and passed through a 40 μm cell strainer into a 15-mL conical tube coated with 1% bovine serum albumin. Following filtration, Hoechst dye (1 μg/mL) and Nuclei Fixation Solution (Parse Biosciences, Cat#ECF2103) were added, and samples were incubated on ice for 10 min. Nuclei were sorted by fluorescence-activated cell sorting (FACS) in 1× phosphate buffer (approximately 1×10^6 nuclei per sample), transferred to a new 1% bovine serum albumin–coated 15-mL conical tube, and centrifuged at 200×*g* for 10 min at 4 °C. The supernatant was carefully removed, leaving approximately 1.0 mL above the pellet. Nuclei were permeabilized by adding Nuclei Permeabilization Solution and incubating on ice for 3 min, followed by neutralization with Nuclei Neutralization Buffer and centrifugation at 200×*g* for 10 min at 4 °C. The final pellet was fully resuspended in Nuclei Buffer supplemented with DMSO and stored at −80 °C until library preparation. Single-nucleus RNA-sequencing libraries were generated using the Evercode WT Mini v2 kit (Parse Biosciences, Cat#ECW02010) according to the manufacturer's instructions.

Single-nucleus RNA sequencing analysis

Raw-counts matrices were read into Seurat (v.5) and filtered to cells containing over 500 unique detected genes. One wild-type replicate had poor quality and was excluded from the analyses. Standard normalization, feature selection, and scaling procedures were employed. After principal component analysis and dimension reduction via uniform manifold approximation and projection, cells were annotated by cluster as follows: fibroblasts (*pdgfb*, *col1a1b*), ependymo-radial glia (*gfap*, *sox2*, *slc4a10a*), glutamatergic neurons (*snap25a*, *elavl3*), CSF–contacting neurons (*pkd2l1*), serotonergic neurons (*tph2*), oligodendrocyte precursor cells (*cspg4*, *sema5a*), oligodendrocytes (*mpz*, *mag*), microglia/macrophages (*ptprc*, *mpeg1.1*, *itage.1*, *mrc1b*), T cells (*lck*, *runx3*), and proliferating immune cells (*mki67*, *ptprc*). Within ERGs, differentially expressed genes were computed using a Wilcoxon test and Bonferroni post-hoc adjustment, as implemented in Seurat. Gene set enrichment, based on genes rank ordered by fold change, was computed using the WebGestalt online tool, using the KEGG pathways.

Mouse datasets for both spinal cord astrocytes[37] and fibroblasts[44] were obtained and opened in Seurat. The selected cell populations were then analyzed identically to the zebrafish ependymo-radial glial cells, namely, differential expression via Wilcoxon testing and gene set enrichment analysis via WebGestalt online tools, based on fold-change rank ordering.

Motif analyses

The position probability matrix for each transcription factor (TF) was pulled from the JASPAR vertebrate library and compiled into a dataset which was then fed into FIMO. For this analysis we filtered FIMO hits selecting for $p < 0.001$. This FIMO output was used as the primary dataset for motif analysis. To visualize TF binding site clusters, a custom python script (plot_fimo_clusters.py) was developed. This script reads the FIMO output, computes the midpoint of each hit, and converts it into a coordinate system relative to the *gata4* TSS. Because *gata4* is located on the minus strand, upstream regions are represented as positive distances from the TSS (0) along the x axis. To identify local motif clusters, the script performs a sliding-window analysis across the upstream regulatory regions. For the *gata4* upstream region, a 250-bp window with a 50-bp step size was used. Windows were classified as cluster-like if they contained >3 motif hits, >2 TF families, and at least one motif with $q \leq 0.05$. For the *loxl2b* upstream region, more stringent criteria were applied because of the noisier motif distribution, using a 150-bp window with a 100-bp step size and requiring ≥10 motif hits, ≥5 TF families, and at least one motif with $q \leq 0.005$.

QUANTIFICATION AND STATISTICAL ANALYSIS

Tissue bridge quantification

Tissue bridge diameter was quantified in ImageJ/FIJI. For each fish, 3–5 20 μm sections containing the thickest portion of the tissue bridge were analyzed. Lesion diameter was measured and normalized to the uninjured spinal cord diameter caudal to the lesion.

Loxl2 immunostaining quantification

A 300 μm region of interest (ROI) was centered on the edge of the spinal cord stump, guided by GFAP signal. The FIJI "Analyze Particles" function was used to determine the percentage area occupied by Loxl2 within the ROI. Measurements were performed blinded, using at least three sections per zebrafish, and the values were averaged to yield a single value for each animal.

Mean gray value analysis

Spinal cord images of TMR-O– and TMR-NB–treated fish were acquired under identical confocal settings (Galvano scan mode; integration = 1; dwell time = 0.4 μs; 561 nm laser at 0.639%; z-step = 3.4 μm; 7 z-steps). Maximum intensity projections were generated in FIJI. A polygonal ROI was drawn around the lesion site, excluding bone, and Mean Gray Value was measured using the FIJI "Measure" function. For each animal, 2–5 sections were analyzed.

For quantifications in DMOG- and PX-478 treated larvae, anesthetized animals were positioned on their side in an imaging dish. Images for quantifications were acquired on the same day using uniform laser power, integration and dwell time with consistent x–y dimensions and z stack parameters across samples. A uniform ROI was set around the Gata4 signal (excluding any notochord or epidermis) and mean gray value was obtained using FIJI.

Quantification of Syt2a+ axons

Confocal images of biocytin and Syt2a labeled axons were acquired immediately posterior to the lesion site at 4wpi using a Nikon Plan Apo 60× oil objective, NA = 1.42. Three sections per specimen were imaged, and consistent imaging settings were used throughout the experiment. Images were processed and analyzed using Nikon Elements GA3. A custom GA3 recipe was created to preprocess and quantify images. Preprocessing included background subtraction using a rolling ball algorithm, uniform contrast enhancement, and thresholding. Axonal surface area was calculated for each axon, and the area occupied by Syt2a signal was quantified based on Syt2a-positive signal directly contacting the axonal surface.

Colocalization analyses

For non-nuclear colocalization analyses, images from 2 to 5 tissue sections per animal were processed in Nikon NIS-Elements AR. Within each measurement set, channels were uniformly thresholded to generate binary masks for each signal. Manders' colocalization coefficients were then calculated from the thresholded images, multiplied by 100, and reported as percent overlap.

For nuclear-based colocalization measurements (e.g., EdU, PCNA, Sox2), nuclei within 450 μm of the lesion site were manually counted across 2–5 sections per animal in Nikon NIS-Elements AR (EdU^+EGFP^+) or Fiji ($PCNA^+Sox2^+$), and the proportion of nuclei overlapping the signal of interest was quantified.

In situ hybridization quantification

In situ hybridization signal was quantified from 2 to 5 sections per animal using a custom Python script that extracted mean RGB values for each image within a defined ROI. Average intensity values for the red, green, and blue channels were calculated for each sample. RGB triplets were plotted in 3D color space to visualize distribution patterns. A consistent inverse correlation was observed between signal strength and red + green (R + G) intensity, reflecting the deeper blue/purple chromogenic product. Principal component analysis confirmed that R + G intensity captured the primary variance associated with *in situ* hybridization signal. Thus, R + G values were used for subsequent statistical comparisons.

AFOG and Picrosirius Red staining quantification

AFOG- and Picrosirius Red-stained sections (3–5 per animal) were imaged and scored blindly by two investigators and assigned to four bins: 0 = no detectable aniline blue staining, 1 = minimal staining, 2 = moderate staining, and 3 = maximal staining.

Statistical analysis

Spinal cord transection surgeries and regeneration analyses were performed in a blinded manner whenever possible. Experiments were repeated 2–4 times using independent clutches of animals. Unless otherwise indicated, each data point represents a single animal, and n represents the number of animals analyzed. Exact sample sizes (n), statistical tests, p values are provided in the corresponding figures or figure legends. All individual data points are shown in the graphs. For violin plots, dashed lines denote medians and dotted lines denote the 25th and 75th percentiles. All statistical analyses were performed using GraphPad Prism v10.3.1. For comparisons between two groups, data were assessed for normality, and either Welch's t test or the nonparametric Mann–Whitney test was used as appropriate. Paired t-tests were used for paired comparisons where indicated. two-way ANOVA was used to assess the effects of genotype and time and their interaction on swim performance. Fisher's exact test was used to compare categorical outcomes, including collagen deposition in AFOG- and Picrosirius Red-stained sections.